HHS Public Access

Author manuscript

Cancer Cell. Author manuscript; available in PMC 2020 October 05.

Published in final edited form as:

Cancer Cell. 2019 June 10; 35(6): 916–931.e9. doi:10.1016/j.ccell.2019.05.002.

Non-oncogene Addiction to SIRT3 Plays a Critical Role in Lymphomagenesis

Meng Li[1], **Ying-Ling Chiang**[2], **Costas A. Lyssiotis**[3], **Matthew R. Teater**[1], **Jun Young Hong**[2], **Hao Shen**[1], **Ling Wang**[1], **Jing Hu**[2], **Hui Jing**[2], **Zhengming Chen**[4], **Neeraj Jain**[7], **Cihangir Duy**[1], **Sucharita J. Mistry**[1], **Leandro Cerchietti**[1], **Justin R. Cross**[5], **Lewis C. Cantley**[6], **Michael R. Green**[7], **Hening Lin**[2,*], **Ari M. Melnick**[1,8,*]

[1]Department of Medicine, Division of Hematology & Medical Oncology, Weill Cornell Medicine, New York, New York 10065, USA

[2]Department of Chemistry and Chemical Biology, Howard Hughes Medical Institute, Cornell University, Ithaca, NY, 14853, USA

[3]Department of Molecular and Integrative Physiology, University of Michigan Medical School, Ann Arbor, Michigan 48109, USA

[4]Division of Biostatistics and Epidemiology, Weill Cornell Medicine, New York, NY, 10021, USA

[5]Cancer Biology and Genetics Program, Memorial Sloan-Kettering Cancer Center, New York, NY 10065, USA

[6]Meyer Cancer Center, Weill Cornell Medicine, New York, NY 10065, USA

[7]Department of Lymphoma/Myeloma, University of Texas MD Anderson Cancer Center, Houston, TX 77005, USA

[8]Lead contact

Summary

Diffuse large B-cell lymphomas (DLBCLs) are genetically heterogeneous and highly proliferative neoplasms derived from germinal center (GC) B-cells. Herein, we show that DLBCLs are dependent on mitochondrial lysine deacetylase SIRT3 for proliferation, survival, self-renewal, and tumor growth *in vivo* regardless of disease subtype and genetics. SIRT3 knockout attenuated B-cell lymphomagenesis in *VavP-Bcl2* mice without affecting normal GC formation. Mechanistically, SIRT3 depletion impaired glutamine flux to the TCA cycle via glutamate dehydrogenase and reduction in acetyl-CoA pools, which in turn induce autophagy and cell death.

[*]**Correspondence: Ari Melnick, MD) (Lead Contact)**, Department of Medicine, Division of Hematology and Medical Oncology, Weill Cornell Medicine, New York, NY 10021, USA, Tel: 212-746-7643, amm2014@med.cornell.edu; Hening Lin PhD, Howard Hughes Medical Institute, Department of Chemistry and Chemical Biology, Cornell University, Ithaca, NY, 14853, USA, Tel: 607-255-4650, hl379@cornell.edu.

AUTHOR CONTRIBUTIONS

Conceptualization, A.M., H.L. and M.L.; Project Administration, M.L. and A.M.; Investigation, M.L., H.S., L.W., C.L., and J.C.; Formal Analysis, M.L., M.T. (RNA-seq and metabolomics), C.L.(metabolic flux), Z.C. (microarray and survival), N.J. and M.G. (DNA copy number); Methodology and Resources H.L., Y-L.C., J.Y.H., J.H. and H.J (small molecule inhibitor synthesis and *in vitro* assays).; Resources, L.C. and C.D.; Writing, M.L., A.M., S.M., H.L., and C.D.; Supervision, L.C., H.L. and A.M..

DECLARATION OF INTEREST

A M. receives research funding from Janssen and has consulted for Epizyme and Constellation.

We developed a mitochondrial-targeted Class I sirtuin inhibitor, YC8-02, that phenocopied the effects of SIRT3 depletion and killed DLBCL cells. SIRT3 is thus a metabolic non-oncogene addiction and therapeutic target for DLBCLs.

Keywords

SIRT3; Cancer metabolism; Glutaminolysis; TCA cycle; Autophagy; YC8-02 inhibitor; DLBCL; GDH

Introduction

Diffuse large B-cell lymphomas (DLBCLs) are an aggressive and heterogeneous group of diseases from the genetic and molecular standpoints. Though R-CHOP chemoimmunotherapy has improved DLBCL clinical outcomes, approximately 40% of patients relapse or are refractory to their treatments (Basso and Dalla-Favera, 2015; Intlekofer and Younes, 2014). DLBCLs manifest more than 150 recurrent somatic mutations and are highly genetically complex (Reddy et al., 2017). Despite this mutational diversity, there are general molecular mechanisms that drive malignant phenotype across broader cross-sections of DLBCL patients and serve as a source of non-oncogene addiction (dependencies on non-mutated genes). Targeting specific genes contributing to non-oncogene addiction may provide an attractive strategy for therapeutic vulnerability in lymphomas independent of their genetics (Luo et al., 2009).

One form of non-oncogene addiction in cancer is the dependency of tumors on particular metabolic pathways for their survival and proliferation (Luo et al., 2009; Pavlova and Thompson, 2016). It is notable that DLBCLs are highly proliferative and metabolically active tumors that must fulfill significant requirements for energy and metabolic precursors. DLBCLs rely on aerobic glycolysis to generate energy and metabolic precursors, which limits the production of metabolic precursors through the tricarboxylic acid (TCA) cycle via glucose (Caro et al., 2012; Le et al., 2012). Instead, lymphoma cells engage anaplerotic programs to supply the TCA cycle with metabolites for synthesis of fatty acids, amino acids and nucleotides (Caro et al., 2012; Le et al., 2012). However, the mechanisms that control the activity and role of these different metabolic pathways in DLBCL are poorly understood.

Sirtuin family proteins have been implicated in mediating cancer adaptive pathways relevant to metabolism and gene expression, some having oncogenic and others tumor suppressor functions (Chalkiadaki and Guarente, 2015; Houtkooper et al., 2012). Sirtuins are evolutionally conserved nicotinamide adenine dinucleotide (NAD^+)-dependent lysine deacetylases. In mammals, seven sirtuin members (SIRT1-SIRT7) possess various enzymatic activities including lysine deacetylation, desuccinylation and defattyacylation. Depletion of NAD^+ induces cell death in hematologic cancer cells, which implicates NAD^+ dependent sirtuins as important for survival (Nahimana et al., 2009). Prior reports suggest that SIRT1 may play both oncogenic and tumor suppressive functions in lymphoma. *Sirt1*$^{+/-}$ *Trp53*$^{+/-}$ mice tend to develop lymphomas (Oberdoerffer et al., 2008), while inhibition of SIRT1 mediated deacetylation of BCL6 and p53 may promote lymphoma cell death (Bereshchenko

et al., 2002; Heltweg et al., 2006). Functions of other sirtuins in lymphomas largely remain unknown, which may lead to better understanding of DLBCLs and therapeutic options.

Results

DLBCL Cells are Biologically Dependent on SIRT3 Regardless of Disease Subtype

We performed an shRNA survey of the importance of the seven sirtuin family members in two DLBCL cell lines. We observed that SIRT3 was the most robustly required, although SIRT5 and SIRT7 depletion was also deleterious (Figures S1A–S1B). SIRT3 is generally considered a tumor suppressor in solid tumors (Finley et al., 2011; Haigis et al., 2012) but its function in DLBCL has not been systematically explored. To confirm that DLBCLs are dependent on SIRT3, we assembled a panel of eight DLBCL cell lines representing the cell of origin (COO) classification of DLBCL: germinal center B-cell (GCB) and activated B-cell (ABC) DLBCLs (Alizadeh et al., 2000), as well as DLBCL cells classified as having oxidative phosphorylation (OxPhos) gene expression signatures (Monti et al., 2005). We also included two control solid tumor cell lines, given that SIRT3 may function as a tumor suppressor in these cells (Bell et al., 2011; Haigis et al., 2012). We generated lentiviruses expressing three individual SIRT3 shRNAs or control shRNA with yellow fluorescent protein (YFP) (Figure S1C). All DLBCL cell lines manifested significant depletion of YFP^+ cells expressing SIRT3 shRNA as compared to control (Figure 1A). In contrast, depletion of SIRT3 had no significant effects against the solid tumor cells (Figures 1A and S1D). The effect of SIRT3 depletion was partially rescued by co-expressing an shRNA-resistant form of SIRT3 (Figure S1E). Full rescue was not achieved, perhaps because we could not precisely titrate levels of exogenous SIRT3. However, a catalytically dead mutant ($SIRT3^{H248Y}$) failed to rescue, indicating that the enzymatic function of SIRT3 is required for its function in DLBCL (Figure S1E).

SIRT3 is Overexpressed in DLBCLs and Linked to Inferior Clinical Outcome

We compared and contrasted the level of SIRT3 expression in primary DLBCL specimens with normal GC B cells, which are the cell of origin of DLBCLs. Analysis of the RNA-seq data from a cohort of 56 DLBCL cases and four normal purified human tonsil GC B-cell ($CD20^+lgD^-CD77^+$) specimens, indicated that SIRT3 mRNA was significantly elevated in DLBCLs compared to GC B cells (Figure 1B). We also observed that SIRT3 protein was consistently more abundant in primary DLBCL specimens and DLBCL cell lines than in GC B cells (Figures 1C and S1F).

We next evaluated the association of the expression of *SIRT3* with clinical outcome in 757 patients corresponding to four publicly available DLBCL gene expression profiling cohorts (Hummel et al., 2006; Jais et al., 2008; Lenz et al., 2008a; Shaknovich et al., 2010). The optimal cutoff for *SIRT3* expression was defined as the point with the most significant log-rank p value split (Budczies et al., 2012). We observed that higher *SIRT3* expression was significantly associated with inferior overall survival (Figure 1D). We lacked statistical power for a multivariate analysis since the annotation of clinical features was not concordant between these cohorts. No other sirtuin family members whose expression was consistently linked to inferior outcome (not shown).

SIRT3 Maintains DLBCL Proliferation, Survival and Self-renewal

To understand the nature of SIRT3 dependency, we performed a series of phenotypic assays in DLBCL cells. Loss of SIRT3 significantly inhibited cell proliferation compared to control cells as determined by cell counts (Figure 2A). Tracking intravital dye dilution over 5 days, we observed that YFP^+ cells with SIRT3 shRNAs but not control shRNA retained more dye compared to YFP-(uninfected) cells (Figure S2A), indicating inhibition of cell proliferation. In cell cycle progression assays using BrdU labeling, SIRT3 shRNAs caused a consistent reduction of YFP^+S-phase cells but expansion of cells in G_0/G_1 as compared to YFP^- cells (Figures 2B–2C). To study effects on cell death, SIRT3 shRNA transduced cells were stained with Annexin V and DAPI and analyzed by flow-cytometry at two timepoints. There was no induction of cell death 3 days after shRNA transduction. However, by day 10, we observed 2-4 folds increase in apoptosis in SIRT3 depleted vs control cells (Figure S2B). Finally, we observed significant loss self-renewal ability in colony-forming assay after SIRT3 shRNA transduction (Figures 2D and S2C).

SIRT3 is Required to Maintain the Growth of Lymphomas *In vivo*

To determine whether SIRT3 is required for the growth of DLBCL *in vivo,* we used a lentivirus vector expressing doxycycline inducible shRNA and GFP, which indicates the cells with shRNA expression after doxycycline induction. Karpas 422 cells were transduced with the inducible vectors expressing control or two independent SIRT3 shRNAs, then implanted in mice. shRNA expression was induced when tumors grew to 50-100 mm^3 (Figure 2E). We observed that the expression of SIRT3 shRNAs significantly suppressed tumor growth as compared to controls (Figure 2F). Although all tumors started with around 70% GFP^+ cells, tumors expression SIRT3 shRNA, but not control, were severely depleted of GFP^+ cells after doxycycline exposure (Figure 2G). We administered BrdU to these mice prior to euthanasia and observed that viable GFP^+ cells with SIRT3 vs control shRNA contained reduced proportion of S phase and increased fraction of G_0/G_1 phase populations, whereas GFP^- cells exhibited no perturbation (Figure 2H).

SIRT3 is Dispensable for GC B cell Formation *In vivo*

Many lymphoma oncoproteins (e.g. BCL6 and EZH2) also play essential roles in GC formation (Beguelin et al., 2013; Dent et al., 1997). Therefore, we evaluated the role of *Sirt3* in GC formation in constitutive $Sirt3^{-/-}$ mice, which are viable and healthy under normal conditions (Hirschey et al., 2010). GC formation was induced in $Sirt3^{-/-}$ and wild-type control mice by immunization with a T-cell dependent antigen. Mice were sacrificed 10 days later at the peak of the GC reaction and spleens examined by immunohistochemistry (IHC) and flow-cytometry. The splenic architecture of $Sirt3^{-/-}$ mice was unperturbed as compared with wild-type mice. Staining of spleen sections using the GC B-cell specific lectin peanut agglutinin (PNA) (Figure 3A) showed no difference in the number of GCs (Figure 3B), the total spleen area occupied by GCs (Figure 3C) or the average area of each GC (Figure 3D). Immunophenotyping likewise yielded similar percentage of GC B cells ($B220^+FAS^+CD38^{low}$) in $Sirt3^{-/-}$ vs wild-type mice (Figures 3E–3F and S3A). No significant changes were observed among follicular B and marginal zone B cells (Figures 3E–3F and S3B).

SIRT3 is thus dispensable for GC formation and is an acquired adaptation associated with malignant lymphomas.

SIRT3 is Required to Maintain the TCA cycle in DLBCLs

Cancer cells undergo metabolic reprogramming to meet their energetic and biosynthetic demands (Hanahan and Weinberg, 2011; Pavlova and Thompson, 2016). SIRT3 localizes in mitochondria and deacetylates various metabolic enzymes (Baeza et al., 2016; Hebert et al., 2013; Yang et al., 2016). Thus, it is plausible that DLBCL dependency on SIRT3 is linked to effects on mitochondrial metabolic pathways. To understand SIRT3 mechanism of action in DLBCL, we performed metabolomic profiling in Karpas 422 cells after transduction with SIRT3 or control shRNA. Unsupervised hierarchical clustering analysis indicated a clear distinction between metabolic profiles in SIRT3 vs control shRNA DLBCL cells (Figure 4A).

To determine which metabolic pathways were affected, we performed a pathway enrichment analysis using >3000 annotated pathways from 11 databases (Kamburov et al., 2011). This analysis indicated major reduction of TCA metabolites after SIRT3 knockdown, as well as reduction of pyruvate and alanine metabolic pathways, whereas glycolysis and glucose metabolism were induced (Figure 4B). We observed depletion of key TCA cycle metabolites such as citrate, α-ketoglutarate (αKG), succinate, fumarate, and malate (Figure 4C). We also observed accumulation of glutamate, reduction in downstream glycolytic metabolites (3-phosphoglyceric acid, pyruvate, alanine and lactate) and increase of upstream glycolysis metabolites (glucose 6-phophate and fructose 6-phosphate) (Figure 4C). TCA cycle defects are generally accompanied with decrease of acetyl-coenzyme A (AcCoA) production (Eisenberg et al., 2014; Martinez-Reyes et al., 2016; Schroeder et al., 2014). Indeed, we observed significant reduction of AcCoA vs total CoA after SIRT3 depletion (Figure 4D). The impact of acetyl-CoA reduction was underlined by the marked decrease in acetylated histone 3 (Ac-H3) (Figure 4E). These effects were generally reproducible in a second DLBCL cell line (Figures S4A–C).

Perturbation of the TCA Cycle by SIRT3 shRNAs Activates Autophagy

Impairment of the TCA cycle and AcCoA levels is reported to induce autophagy (Eisenberg et al., 2014; Martinez-Reyes et al., 2016), perhaps because cells must obtain metabolic precursors from alternative sources. Upon induction of autophagy, LC3I is conjugated to phosphatidylethanolamine to form LC3II, resulting in increased LC3II/LC3I ratios (Klionsky et al., 2016; Noda and Inagaki, 2015). We observed that SIRT3 depletion caused increased LC3II/LC3I ratios and reduction of p62 protein, which is degraded upon induction of autophagy (Klionsky et al., 2016; Noda and Inagaki, 2015), in DLBCL cell lines (Figure 5A). We also used a fluorescent reporter (mCherry-EGFP-LC3B) to quantify autophagic flux, whereby autophagy active cells manifest $EGFP^{low}$ and $mCherry^{high}$ signals (Gump et al., 2014; Klionsky et al., 2016; Noda and Inagaki, 2015). SIRT3 knockdown enhanced abundance of $EGFP^{low}mCherry^{high}$ cells (Figure 5B) and autophagy active cells showed higher mCherry/EGFP signal across multiple cell lines (Figures 5C–5E and S5A). Activation of autophagy by SIRT3 depletion was partially rescued by re-expression of

SIRT3, but not SIRT3^{H248Y} (Figure S5B). Therefore, SIRT3 suppresses autophagy through its protein deacetylase activity.

To test for actual link of autophagy with impaired TCA cycle induced by SIRT3 depletion, we used dimethyl-αKG (DMKG) to replenish TCA cycle metabolism (Eisenberg et al., 2014). We observed that DMKG rescued LC3II/LC3I ratios (i.e. autophagy) in DLBCL cells (Figure 5F). In addition, restoring the TCA cycle with DMKG and methyl-pyruvate (MP) (Herranz et al., 2015; Son et al., 2013) rescued proliferation arrest caused by SIRT3 depletion (Figures 5G, S5C–S5D). Whereas DMKG alone rescued SIRT3 depleted Karpas 422 (Figure 5G) and OCI-LY1 (Figure S5C) cells, HBL1 cells required both DMKG and MP (Figure S5D) pointing to a partial dependency of HBL1 cells on the pyruvate pathway. To test if autophagy contributes to proliferation arrest caused by SIRT3 depletion, we knocked down ATG5, which is required for formation of autophagosomes (Noda and Inagaki, 2015; Takamura et al., 2011). As expected, ATG5 shRNA impaired autophagy in DLBCL cells (Figure 5H). However, we also observed that ATG5 depleted cells manifested resistance to SIRT3 knockdown (Figure 5I). Hence proliferation arrest induced by SIRT3 depletion in DLBCL is at least in part caused by autophagy that is triggered by impairment of the TCA cycle.

These data suggest that autophagy has a tumor suppressor effect in DLBCL. Indeed by examining the genetic profiles of 694 DLBCL samples (Green et al., 2014) we observed that 6q deletion, which contains the *ATG5* locus, was one of most highly recurrent genetic alterations (17% of cases, Figure S5E). We confirmed this observation in an independent cohort of patients (Chapuy et al., 2018). Strikingly, *ATG5* is within the 6q21 region that is most reproducibly deleted. Analysis of gene expression in the same patients revealed that *ATG5* deletion is accompanied by significant reduction of *ATG5* transcript abundance (Figure S5F), providing genetic evidence that autophagy is a tumor suppressive in the DLBCL context.

SIRT3 Drives Anaplerotic Glutaminolysis to Power the TCA cycle in DLBCL Cells

B-cell lymphomas use both glucose and glutamine to power the TCA cycle to generate energy and metabolic precursors (Caro et al., 2012; Le et al., 2012). Hence, we considered two possible explanations for loss of TCA cycle function: i) impaired glycolysis, or ii) block of anaplerotic reactions for glutamate/glutamine usage. To determine which is occurring, we performed metabolic tracing studies using ^{13}C-labeled glutamine ([U-^{13}C5] glutamine) and glucose ([U-^{13}C6] glucose). Glutamine is used in TCA cycle after being transformed into glutamate, which is then converted to αKG by glutamate dehydrogenase (GDH). In the TCA cycle, αKG can be used through de-carboxylation to produce succinate (forward) or carboxylation to form citrate (reverse) (Figure 6A). Analysis of ^{13}C glutamine labeled metabolites after SIRT3 knockdown showed decreased contributions of ^{13}C from glutamine to both forward (M+4-succinate, fumarate, malate and aspartate) and reverse TCA cycle (M +5-citrate, M+3-malate and -aspartate, Figures 6A–6B). In contrast, ^{13}C glucose labeling experiments revealed increased ^{13}C incorporation into the TCA cycle metabolites after SIRT3 knockdown (Figures S6A–S6B). At the same time, there was reduction of ^{13}C incorporation to alternative glycolysis pathway metabolites including 3-PG, serine, alanine

and lactate (Figures S6A–S6B). The results were further validated in ^{13}C-glutamine and ^{13}C-glucose tracing studies in OCI-LY1 cells, confirming that SIRT3 depletion impairs glutamine entry into the TCA cycle and increases utilization of glucose (Figures S6C–S6D).

Glutamine Dehydrogenase is a Key Downstream Target of SIRT3 in DLBCL Cells

We next explored the direct mechanism through which SIRT3 drives glutamine entry to the TCA cycle. Protein acetylation plays an important role in regulating the activity of metabolic pathways (Baeza et al., 2016; Hebert et al., 2013; Yang et al., 2016). As expected, SIRT3 depletion caused an increase in mitochondrial protein acetylation in DLBCL cells (Figure S6E). We then tested whether GDH, which converts glutamate to αKG to enter the TCA cycle, could be *a* key target of SIRT3 deacetylation (Lombard et al., 2007). For this, we expressed FLAG tagged GDH in three DLBCL cell lines with SIRT3 or control shRNAs then performed FLAG-IP in these cells followed by acetyl-lysine immunoblot. In all cases, SIRT3 depletion induced GDH hyperacetylation (Figure 6C). We also performed GDH enzymatic activity assays with DLBCL cell lysates after SIRT3 knockdown and observed decreased GDH activity in accordance with the notion that acetylation impairs its enzymatic activity (Figures 6D and S6F). To determine whether GDH activity is critical to the SIRT3 phenotype, we overexpressed GDH in SIRT3 depleted cells and found that it prevented induction of autophagy after SIRT3 knockdown (LC3II/LC3I ratios, Figure 6E). GDH overexpression also significantly rescued SIRT3 cell proliferation and survival effects (Figures 6F–6G and S6G). Reciprocally, GDH knockdown induced proliferation arrest and activation of autophagy in DLBCL cells, similar to what we observe with SIRT3 knockdown (Figures S6H–S6I). Therefore, deacetylation and induction of GDH activity is critical to the effect of SIRT3 in DLBCL cells.

SIRT3 is Required for Lymphomagenesis *In vivo*

To determine whether SIRT3 might be required to support the malignant transformation of GC B cells into lymphomas and not just maintaining proliferation of established DLBCL cells, we crossed *Sirt3*$^{-/-}$ mice with *VavP-Bcl2* transgenic mice, which develop GC derived lymphomas (Egle et al., 2004). *VavP-Bcl2;Sirt3*$^{+/+}$ mice developed lymphoma by 6 months of age, manifesting as gross enlargement and distortion of lymphoid follicles and aberrant GC structures in PNA and B220 IHC staining (Figure S7A). In contrast, *VavP-Bcl2;Sirt3*$^{-/-}$ mice of similar age still maintained follicle structures with less invasive outgrowth of B cells (Figure S7A). An additional cohort of mice generated by transplanting bone marrow cells from *VavP-Bcl2;Sirt3*$^{-/-}$ and *VavP-Bcl2;Sirt3*$^{+/+}$ mice into lethally irradiated recipients were sacrificed ~110 days after transplant to determine whether incipient lymphomas were developing. Mice transplanted with *VavP-Bcl2;Sirt3*$^{-/-}$ cells displayed significantly less splenomegaly than (Figure 7A), but similar body weight to (Figure S7B), those transplanted with *VavP-Bcl2;Sirt3*$^{+/+}$ cells. As expected, mice transplanted with *VavP-Bcl2;Sirt3*$^{-/-}$ cells developed systemic lymphoma with infiltration of highly proliferative B cells consistent with DLBCL in multiple organs including lung and liver (Figures 7B and S7C). In marked contrast, mice transplanted with *VavP-Bcl2;Sirt3*$^{-/-}$ cells had no evidence of systemic lymphoma (Figures 7B and S7C) and manifested significantly improved survival vs those transplanted with *VavP-Bcl2;Sirt3*$^{+/+}$ cells (Figure 7C). Hence SIRT3 contributes to

lymphomagenesis *in vivo*, underlining a critical role for its metabolic effects in B-cell transformation.

Loss of SIRT3 Impaired the TCA cycle Metabolism and Induced Autophagy in Primary Lymphomas *In vivo*

To determine whether SIRT3 mediated similar effects on metabolism in primary lymphomas in vivo, we enriched for $B220^+$ cells from spleens of *VavP-Bcl2;Sirt3*$^{+/+}$ and *VavP-Bcl2;Sirt3*$^{-/-}$ mice for metabolic profiling, matching mice for gender and age. Similar to human cell lines, absence of SIRT3 caused a reduction in TCA metabolites, pyruvate metabolism, and glucagon signaling (Figure 7D). Because direct measurement of AcCoA was impossible in these specimens, we examined Ac-H3, as a surrogate, and observed significantly lower abundance of in *VavP-Bcl2;Sirt3*$^{-/-}$ splenocytes (Figure S7E). We accordingly also observed higher ratio of LC3II/LC3I in *VavP-Bcl2;Sirt3*$^{-/-}$ splenocytes (Figures 7E–7F), which was inversely correlated to p62 abundance (Figure 7G). Moreover, spleen/body weight were negatively correlated with autophagy (Figure S7F), which is in accordance with the proposed tumor suppressor function of autophagy (Kenific and Debnath, 2015), suggesting that SIRT3 overcomes this mechanism to support the growth of B-cell lymphomas.

Therapeutic Targeting of DLBCL with Small Molecule SIRT3 Inhibitors

Given its important role in proliferation and survival of DLBCL cells but being dispensable to normal cells, SIRT3 could serve as an attractive drug target. We developed a series of small molecules including a SIRT2 selective thiomyristoyl lysine compound called TM (Jing et al., 2016) and Biotin-TM3 (selective to SIRT1 and SIRT2). To improve SIRT3 inhibition, we developed a compound called JH-T4 that can inhibit all three Class I sirtuins at micro- to nanomolar concentrations in biochemical enzymatic assays (Figures 8A–8B and S8A). To achieve superior penetration into mitochondria, JH-T4 was modified by replacing the benzyl carbamoyl group with a triphenylphosphonium (TPP) mitochondrial targeting moiety to yield the compound, YC8-02 (Figures 8A–8B and S8B–S8C). Compared to JH-T4, YC8-02 manifested increased ratio of mitochondria to total cell concentration, as measured by mass spectrometry in purified mitochondria extracts and total cell lysates (Figure S8D). YC8-02 was also unexpectedly more efficient than JH-T4 at inhibiting SIRT3 in *in vitro* biochemical assays (Figures 8B and S8C).

We next evaluated the effect of these compounds on the viability and the proliferation of DLBCL cell lines. YC8-02 was the most effective one (Figures 8C–8D, S8E–S8F), JH-T4 lacks the TPP motif and was much less active, Biotin-TM3 does not target SIRT3 and was inactive in these assays. Therefore, mitochondrial targeting of SIRT3 was critical to the YC8-02 effect in DLBCLs. Moreover, YC8-02 effects were selective to DLBCL vs human solid tumor cell lines or cord blood cells (Figures S8G–S8H).

To validate that the effects of YC8-02 were linked to suppression of SIRT3, we first observed that treatment of DLBCL cells with YC8-02 increased mitochondrial protein acetylation (Figure 8E). Moreover, YC8-02, but not JH-T4, inhibited GDH activity (Figure 8F) and induced autophagy (Figure 8G) in DLBCL cells. Finally, we performed

metabolomic profiling in Karpas 422 cells treated with YC8-02, JH-T4 or vehicle. YC8-02 manifested a distinct profile as compared to JH-T4 and vehicle (Figure 8H). YC8-02 induced greater metabolic perturbation (95 metabolites down and 93 up, $p<0.1$, $logFC>0.3$) than JH-T4 (34 down and 35 up, $p<0.1$, $logFC>0.3$). YC8-02 but not JH-T4 treatment caused reduction of TCA cycle metabolites as well as pyruvate metabolism, alanine biosynthesis and glutaminolysis (Figure 8I). Using an additional quantitative approach, YC8-02 but not JH-T4 enriched for metabolic pathways suppressed by SIRT3 depletion, indicating that the active compound could phenocopy loss of SIRT3 (Figure S8I). We next tested if YC8-02 could suppress lymphoma growth *in vivo*. We first assayed toxicity by treating C57BL/6 mice with 30 mg/kg of YC8-02 or vehicle over five days and observed no evidence of discomfort or weight loss (Figure S8J). The same dose of YC8-02 was then used to treat NOD/SCID mice bearing DLBCL xenografts from Karpas 422 cells, in two five-day pulses. We observed that YC8-02 caused regression of the tumors during the time mice were receiving drug. The suppressive effects persisted for several days after the treatments until the mice were sacrificed (Figure 8J). Lastly, we tested another reported SIRT3 selective inhibitor, compound#8 (Mahajan et al., 2014), which although is less potent than YC8-02 is relatively selective to SIRT3 *in vitro* (Figure S8K). Compound#8 also reduced DLBCL cell viability (Figure S8L) and triggered activation of autophagy (Figure S8M). Collectively, these data indicate that SIRT3 is a therapeutic target in DLBCL and support the rationale for development of clinical grade SIRT3 selective inhibitors.

Discussion

Herein, we provide evidence that SIRT3 is a metabolic, non-oncogene dependency in DLBCL where it is required to maintain the accelerated and sustained metabolic needs of these rapidly dividing and growing tumors. SIRT3 dependency is independent of genetic background and DLBCL subtype, indicating that this is a more generalized biological feature of this disease. Pro-oncogenic effects of SIRT3 were also noted in certain tumor cell lines such as oral and bladder cancers (Chen et al., 2014). Two other studies explored SIRT3 knockdown in B-cell lymphoma cell lines but did not note its pro-oncogenic role (Yu et al., 2016; Yuan et al., 2017). The most likely explanation for this is the use of transient siRNA by one report (Yu et al., 2016) and the use of antibiotic selection in the other (Yuan et al., 2017), which can yield selection of resistant clones. Other studies have reported a tumor suppressor function for SIRT3 for example in breast and ovarian cancers (Bell et al., 2011; Finley et al., 2011), where loss of SIRT3 stabilized HIF1α (hypoxia inducible factor 1α), leading to transcription of glycolytic genes and induction of the Warburg effect. Hence the putative oncogenic and tumor-suppressive roles of SIRT3 are context-specific and may be linked to how its downstream functions play into malignant transformation in different tissues.

Along these lines, it is worth noting that SIRT3 was dispensable for the normal GC B cells from which DLBCLs arise. Like DLBCLs, normal GC B cells also have extreme metabolic needs given their rapid proliferation (Boothby and Rickert, 2017; Ersching et al., 2017; Jellusova et al., 2017). Yet in GC reactions, proliferation is self-limited. When B cells are activated to enter the GC proliferative zone, they first undergo a brief metabolic charging phase when they accumulate metabolic precursors but do not replicate (Boothby and Rickert,

2017; Ersching et al., 2017; Jellusova et al., 2017; Mesin et al., 2016). This anabolic program is shut down during the GC B cell proliferative burst, and depletion of nutrients is believed to limit GC B cell proliferation (Boothby and Rickert, 2017; Jellusova et al., 2017; Mesin et al., 2016). Strictly compartmentalizing anabolic growth from rapid proliferation in the GC may help to limit malignant transformation. Hence, it is tempting to speculate that upregulation of SIRT3 contributes to lymphomagenesis by reprogramming GC B cells to overcome this barrier between metabolic charging and proliferation by enabling B cells to more efficiently metabolize nutrients through anaplerotic pathways.

We find that SIRT3 drives anaplerotic glutaminolysis to fuel the TCA cycle in DLBCL cells independent of whether DLBCLs are of the GCB or ABC subtypes (Alizadeh et al., 2000) or the OxPhos or B cell receptor (BCR) dependent categories (Monti et al., 2005). The OxPhos-DLBCLs can use fatty acids as a source for the TCA cycle and oxidative phosphorylation while the BCR-DLBCLs are more efficient at glycolysis (Caro et al., 2012). Despite these nuances, both the OxPhos and BCR subtypes use glutamine to fuel the TCA cycle (Caro et al., 2012). Hence our results provide the basis to understand the overarching glutamine dependency across DLBCL subtypes, which is mediated in large part through SIRT3 deacetylation of GDH. SIRT3 is thus a critical upstream enzyme in this metabolic cascade. Although our studies point to GDH as a critical target of SIRT3 in DLBCL, these results do not rule out that other SIRT3 TCA substrates downstream of GDH could contribute to its actions (Hebert et al., 2013; Yang et al., 2016). Moreover, SIRT3 may contribute to other biological features of DLBCL through other mitochondrial pathways (Tao et al., 2010). Such considerations warrant further studies.

We present genetic and mechanistic evidence that autophagy is generally a tumor suppressor in DLBCL, downstream of SIRT3. Our results are consistent with data showing autophagy activation under metabolic stress conditions, such as reduction in the TCA cycle activity with decreased AcCoA production (Eisenberg et al., 2014; Marino et al., 2014; Martinez-Reyes et al., 2016). Indeed, autophagy was initially characterized as a tumor suppressing mechanism and mosaic deletion of *Atg5* caused liver tumors in mice (Liu et al., 2017; Pietrocola et al., 2016; Takamura et al., 2011). In contrast, autophagy can also facilitate survival of cancer cells in response to stress by mitigating cellular damage and recycling nutrients to sustain tumor metabolism (Kenific and Debnath, 2015; Kimmelman and White, 2017). Autophagy thus has context-specific roles in cancer, which may depend on the identity and type of proteins that undergo autophagic protein degradation. For example, autophagy may impair DNA replication and metabolic pathways when it induces degradation of proteins important to these functions (Mathew et al., 2014), and can either promote or inhibit apoptosis by degrading particular proteins in response to death stimuli (Gump et al., 2014; Kenific and Debnath, 2015).

The requirement of SIRT3 to maintain the growth and survival of DLBCL cells points toward targeting SIRT3 as a potential therapeutic approach. As all sirtuins require NAD^+ for their enzymatic activity, niacinamide and AP0866 (a NAD^+ biosynthesis inhibitor) were suggested to have therapeutic activity as pan-sirtuin inhibitors in lymphoma patients (Amengual et al., 2013; Ginet et al., 2014; Nahimana et al., 2009). SIRT3 expression rescued NAD^+depletion induced cell death (Yang et al., 2007). The importance of SIRT3 in

DLBCL inspired us to develop the mitochondrial targeted Class I sirtuin inhibitor YC8-02 as a DLBCL therapeutic agent, relevant to a broad cross section of patients including those with inferior clinical outcomes based on current standard of care. Given our finding of autophagy as a tumor suppressor mechanism in DLBCL that is suppressed by SIRT3, it will be important to consider the presence of *ATG5* deletion as a potential source of resistance to SIRT3 inhibitors to aid in patient selection for future clinical trials.

STAR*METHODS

CONTACTS FOR REAGENT AND RESOURCE SHARING

Further information and requests for resources and reagents should be directed to and will be fulfilled by the Lead Contact, Ari Melnick (amm2014@med.cornell.edu).

EXPERIMENTAL MODEL AND SUBJECT DETAILS

Human Tonsil and DLBCL samples—Primary human de-identified leftover tonsil samples and DLBCL samples were obtained and processed under the Institutional Review Board protocols of Weill Cornell Medicine (#0804009762) and the University of Turin (#0081521) after written informed consent, in accordance to the Declaration of Helsinki protocol. Human B cell populations were affinity-purified using standard protocols and GC B cell purity was determined by flow cytometry analysis of surface logD (BD Pharmingen), CD77 (AbD Serotech) and CD38 (BD Pharmingen) (Beguelin et al., 2013).

Mice—The Research Animal Resource Center of the Weill Cornell Medicine approved all mouse procedures. All mice were bred and housed on a 12 hr light/dark cycle. *Sirt3*$^{-/-}$ and 129S1 mice were purchased from Jackson laboratory. 8-14 weeks old female SCID, NOD/SCID and C57BL/6J Cd45.1 mice, purchased from the Jackson lab, were used as recipient mice in xenograft and bone marrow transplantation experiments. *VavP-Bcl2*(Egle et al., 2004) and *Sirt3*$^{-/-}$ mice were crossed to generate *VavP-Bcl2;Sirt3*$^{-/-}$ and *VavP-Bcl2;Sirt3*$^{+/+}$ mice as donor mice for bone marrow transplantation. All mice included in the survival analysis were euthanized when tumors reached maximum size allowed by the animal protocol.

Cell Lines—The DLBCL cell lines, OCI-Ly1 and OCI-Ly7, were grown in Iscove's medium supplemented with 10% FBS and penicillin G/streptomycin; HBL-1, Karpas 422, OCI-LY3, Pfeiffer, SU-DHL4, TMD8 and Toledo were grown in RPMI medium supplemented with 10% FBS, penicillin G/streptomycin, L-glutamine, and HEPES. MCF7, SW480 and HEK-293T cell lines were cultured in DMEM medium supplemented with 10% FBS, 1% penicillin G/streptomycin.

METHOD DETAILS

Generation of lentiviruses—pLKO.1 lentiviral expression vector containing the puromycin resistance gene was used to co-express individual shRNAs with yellow fluorescent protein (YFP). pLKO.1 was further modified for rescue experiments by inserting sequences containing SIRT3^{-}, SIRT3^{H248Y}or GDH. For inducible expression of SIRT3 shRNAs in tumor xenograft studies, we used pLVUTH-KRAB-KM vector with tet-inducible

promotor(Szulc et al., 2006). Autophagy reporter plasmids were derived from control or shSIRT3 pLKO.1 plasmid by adding mCherry-EGFP-LC3 and puromycin resistant genes. The lentiviruses were generated by co-expressing VSV-G and delta-8.9 in HEK-293T cells, and then concentrated using PEG-it (System Biosciences). Cells were infected and cultured for at least three days before adding puromycin for selection and various biological assays.

Cell lysis, immunoblotting and immunoprecipitation—Normal germinal center (GC) B-cells, DLBCL cell lines or primary DLBCL specimens were lysed using RIPA lysis buffer containing complete protease inhibitor cocktail to prepare whole cell lysates or for immunoprecipitation (IP). Whole cell lysates or IP products were resolved by SDS-PAGE, transferred to PVDF membrane (Bio-Rad), and probed with the indicated primary antibodies: anti-SIRT3, anti-GRP75, anti-Acetylated histone 3, anti-Acetylated lysine, anti-LC3 andanti-p62 were from purchased from Cell signaling technology; anti-ACTB, anti-histone 3, and anti-GDH antibodies were purchased from Sigma, Abeam and Proteintech Group respectively. Membranes were then incubated with a corresponding peroxidase-conjugated secondary antibody. Protein signals were detected using enhanced chemiluminescence. Densitometry values were obtained by using ImageJ 1.44o.

RNA-sequencing and analyses—Total RNA was extracted from normal GC B cells (from human tonsils) and DLBCL tumors using Trizol (LifeTechnologies) and RNeasy isolation Kit (Qiagen). RNA concentration was determined using Qubit (LifeTechnologies) and integrity was verified using Agilent 2100 Bioanalyzer (Agilent Technologies). Libraries were generated using the TruSeq RNA sample kit (Illumina). First-strand synthesis was performed using random oligos and SuperscriptIII (Invitrogen). After second-strand synthesis, a 200-bp paired-end library was prepared following the Illumina paired-end library preparation protocol. Pair-end sequencing (PE50) was performed on Illumina HiSeq2000. RNA sequencing results were aligned to hg19, respectively, using STAR (Dobin et al., 2013)and annotated to RefSeq using the Rsubread package(Liao et al., 2013).

Cell proliferation and cell cycle analyses—To evaluate the effects of SIRT3 knockdown on DLBCL cell proliferation, DLBCL and non-DLBCL cell lines were infected with lentiviruses carrying control or SIRT3 shRNAs with yellow fluorescent protein (YFP). Viable YFP^+ cells in control and SIRT3 depleted cells were quantified by flow-cytometry. The change in the percentage of YFP+ population was calculated by normalizing to first time point (5 days post infection). For growth curves, Karpas 422, OCI-LYI and HBL-1 cells expressing control or SIRT3 shRNAs were counted over a period of 7 days by trypan blue exclusion. For assessment of cell proliferation using the intravital fluorescent proliferation dye, infected (YFP^+, with shRNA) or non-infected (YFP^-) Karpas 422 and OCI-LY1 cells were stained with eFIuor 670 (Invitrogen).YFP^+ and YFP^- cells were co-cultured and the dilution of the fluorescent dye in YFP+ and YFP^- cells was monitored after 5 days by flow-cytometry. For cell cycle analyses, infected (YFP^+) and non-infected (YFP^-) cells were analyzed 7-10 days post infection using the BrdU Flow kit (BD Pharmingen™).The data was analyzed using FlowJo software.

Colony-forming assay—Karpas 422, OCI-LY1 and HBL1 cells transduced with control or SIRT3 shRNAs were plated in triplicates in six well plates containing MethoCult™ FI4230 (Stem cell technology). The numbers of colonies were counted from each well after 10-14 days. Colony numbers from SIRT3 depleted cells were normalized to control cells. Data were plotted as an average from three independent experiments. Photographs were taken using a Zeiss Axioskop imaging microscope.

Cell viability assay—Control and SIRT3 shRNA transduced HBL1, Karpas 422 and OCI-LY1 cell lines were washed with PBS and resuspended in staining buffer containing Annexin V-APC (BD biosciences) and DAPI (1μg/ml). The percentage of apoptotic cells was determined by flow-cytometric analyses of Annexin V and DAPI positive cells at days 3 and 10. For cell viability studies using Class I sirtuin inhibitors, DLBCL cells were stained with DAPI (1μg/ml) and percentages of viable cells ($DAPI^-$) were measured by flow-cytometry. The data was analyzed using FlowJo software.

Mice xenograft and *in vivo* cell cycle analyses—Karpas 422 cells infected with pLVUTFI-KRAB lentiviruses with inducible control or SIRT3 shRNAs (infection efficiency was around 70%) were used for the xenograft experiment. Eight-week old female SCID mice housed in barrier environment were subcutaneously injected in the left and right flank with 10^7Karpas 422 cells with control and SIRT3 shRNA respectively. After about 2 weeks when the tumor volumes were around 50-100 mm^3, engrafted mice were given doxycycline in drinking water (1 mg/ml) to induce shRNA and EGFP expression. Tumor volumes were monitored every 2-3 days using electronic digital calipers in 2 dimensions. Tumor volume was calculated using the following formula: tumor volume (mm^3) = (smallest diameter^2 × largest diameter)/2. The mice were sacrificed after three weeks and tumors were harvested. One day before euthanasia, mice were injected with BrdU (50mg/kg) by tail vein injection to label tumor cells for *in vivo* assessment of cell cycle distribution. Tumors were homogenized and ficolled to get single cell suspension for flow-cytometry.

Germinal center assessment—Control *Sirt3*$^{+/+}$ and *Sirt3*$^{-/-}$ mice were immunized intraperitoneally at 8 to 12 weeks of age with 0.5 ml suspension of 2% sheep red blood cell (SRBC) in PBS (Cocalico Biologicals) to induce GC formation. Mice were sacrificed after 10 days and spleens were isolated from control and SIRT3 knockout mice. The spleen sections derived from *Sirt3*$^{+/+}$ and *Sirt3*$^{-/-}$mice were stained by hematoxylin and eosin (FI&E) and peanut agglutinin (PNA) using standard procedures. The number of GCs, the total spleen area occupied by GCs and the average area occupied by the GCs were quantified using ImageJ 1,44o (NIH) software. To determine the percentage of GC B-cell population, single-cell suspensions from spleens derived from *Sirt3*$^{+/+}$ and *Sirt3*$^{-/-}$ mice were stained using the following fluorescent-labeled anti-mouse antibodies: FITC conjugated anti-B220, PE conjugated anti-FAS, APC conjugated anti-CD38 from BD biosciences and analyzed by flow-cytometry. To evaluate follicular and marginal zone B-cell populations, splenic B cells were stained with APC conjugated anti-B220, FITC conjugated anti-CD21 and PE conjugated anti-CD38 from BD biosciences and then analyzed by flow-cytometry. DAPI was used for the exclusion of dead cells. The data was analyzed by FlowJo software.

Metabolomic profiling—The metabolomic studies were done with Karpas 422 and OCI-LY1 cells with control or SIRT3 shRNAs from day 10 post infections after puromycin selection. *In vivo* metabolic profiling was done using $B220^+$ splenocytes from *VavP-Bcl2;Sirt3*$^{+/+}$ and *VavP-Bcl2;Sirt3*$^{+/+}$ mice. $B220^+$ cells were enriched (around 90%) by CD43 negative selection. 4-6 replicates with 10^7 cells per replicate were used in each study. Cell pellets were flash frozen by dry ice and shipped to Metabolon™ for non-targeted metabolomic profiling.

Mass spectrometry analysis of acetyl-CoA and CoA—Karpas 422 cells transduced with control or SIRT3 shRNAs were cultured for 10 days and collected (7-8 million cells per condition) for quantification of AcCoA and total CoA. Cell pellets were lysed with pre-chilled 10% TCA (trichloroacetic acid) and then flash frozen using liquid N2. Samples were vortexed and centrifuged at 14,000 rpm (20000 x g) for 15 minutes at 4°C to remove protein. Acyl-CoAs were purified using an OASIS HLB 96-well plate solid phase extraction (SPE) plate (30 mg) and vacuum manifold. SPE wells were first conditioned with 1 ml of methanol, then equilibrated with 2 x 1 ml of water. Supernatants from cell extracts were then applied to the SPE column. After washing, acyl-CoA was eluted using three successive applications of 0.5 ml of methanol containing 25 mM ammonium acetate. Eluted acyl-CoA was dried for 5 hr in a Genevac EZ-2 Elite using the program FILPC1. Dried samples were resuspended into 110 μL of 50mM Ammonium Acetate pH 4.5 for LC-MS analysis. Acyl-CoA levels were detected using an Agilent 6550 iFunnel Q-TOF LC/MS in positive ionization mode with an Agilent Dual Jet Stream Source.

Measurement of autophagic flux—DLBCL cell lines (HBL1, Karpas 422, 0CI-LY1, Pfeiffer and SU-DHL4) transduced with viruses containing control or SIRT3 shRNA, autophagy reporter plasmids (mCherry-EGFP-LC3) and puromycin resistant gene. Infected cells were first selected with puromycin for at least four days and cells with dual-color florescence were analyzed by flow-cytometry. Cells with high levels of autophagy were defined as those having a high mCherry/EGFP fluorescence ratio as previously describe (Gump et al., 2014).

Metabolic flux assay—For steady state metabolomic analyses, DLBCL cells (Karpas 422 and OCI-LY1) infected with lentiviruses containing control or SIRT3 shRNA were selected with puromycin (1pg/ml) for 7 days, and then grown in a complete media (RPMI, 2 mM glutamine, 10 mM glucose, 10% FBS) for 24 hr. The complete media was changed to ^{13}C labeled medium. To trace glutamine or glucose metabolism in the flux analyses, cells were grown as above and then transferred into glutamine- or glucose-free RPMI containing 10% dialyzed FBS and 2 mM [U-^{13}C5]-glutamine or 10mM [U-^{13}C6]-glucose (Cambridge Isotope Labs) overnight for steady state labeling. Cells were collected by spinning at 300 g for 5 minutes and metabolite extractions were done by adding pre-chilled (−80°C) 80% methanol solution. Each replicate was from extracts of five million cells. Metabolite fractions were collected and analyzed by targeted LC-MS/MS via selected reaction monitoring (SRM) as described (Son et al., 2013).

Measurement of GDH Activity—The GDH activity in DLBCL cells with control or SIRT3 shRNAs was measured using the GDH activity assay kit (Biovision) according to the instructions of the manufacturer.

Immunohistology—Mice organs were fixed in 4% formaldehyde and embedded in paraffin. Deparaffinized slides were antigen retrieved in citrate buffer pH 6.4 and endogenous peroxidase (HRP) activity was blocked by treating the sections with 3% hydrogen peroxide in methanol. Indirect immunohistochemistry was performed with anti-species specific biotinylated secondary antibodies followed by avidin-horseradish peroxidase or avidin-AP and developed by Vector Blue or DAB color substrates (Vector Laboratories). Sections were counterstained with hematoxylin if necessary. The following antibodies were used: biotin-conjugated anti-PNA (Vector Laboratories), biotin-conjugated anti-B220 (Invitrogen RM2615), Ki67 (Vector VPK451). Slides were scanned using a Zeiss Mirax Slide Scanner and photomicrographs were examined using Pannoramic Viewer software. ImageJ 1,44o software (NIH) was used to quantify GC areas.

General methods and materials for class I sirtuin inhibitors—Reagents were obtained from AlfaAesar and Sigma-Aldrich in at the highest purity available and used as supplied. ^{1}H NMR were performed on INOVA 400 spectrometers. Analytic HPLC analysis was carried out on a SHIMADZU LC with Kinetex 5u EVO C18 100A column (100 mm × 4.60 mm, 5 μm, Phenomenex) monitoring at 215 nm and 326 nm. Solvents for analytical HPLC were water with 0.1% trifluoroacetic acid (TFA) as solvent A and acetonitrile with 0.1% TFA as solvent B. Compounds were analyzed at a flow rate of 0.5 ml/min. LC-MS experiments were carried out on a Shimadzu HPLC LC20-AD and ThermoScientific LCQ Fleet with a Kinetex 5 μm EVO C18 100A column (30 × 2.1 mm, 5 μm, Phenomenex) monitoring at 215 and 260 nm with positive mode for detection of mass-to-charge ratio of ions. Solvents for LC-MS were water with 0.1% acetic acid (solvent A) and acetonitrile with 0.1% acetic acid (solvent B) at a flow rate of 0.3 ml/min.

Synthesis of JH-T4—As in Figure S8A, compound 1 was synthesized following a procedure described in the literature (Jing et al., 2016). To a solution of compound 1 (86 mg, 0.17 mmol) and N-methylmorpholine (37.0 μl, 0.34 mmol) in dry dichloromethane (1.7 ml), isobutylchloroformate (38.0 μl, 0.27 mmol) was added dropwisely at 0°C. The reaction mixture was stirred for 30 min at 0°C. 3-Aminophenol (24 mg, 0.22 mmol) was then added at 0°C and the reaction mixture was stirred for 16 hr at room temperature. The solvent was removed under reduced pressure and the resulting residue was dissolved with EtOAc (40 ml) and washed with brine (20 ml). The organic layer was dried over anhydrous sodium sulfate. After removal of the solvents in vacuum, the residue was purified by flash chromatography on silica gel (hexanes:EtOAc = 3:2) to afford the expected compoundT4 (JH-T4) (48 mg, 47 % yield) as a white solid. ^{1}H NMR (400 MHz, CDCb): δ 8.53 (s, 1H), 7.68 (s, 1H), 7.39 (m, 1H), 7.32 (m, 6H), 7.12 (t, J = 8.1 Hz, 1H), 6.86 (d, J = 7.9 Hz, 1H), 6.61 (dd, J = 8.3, 2.3 Hz, 1H), 5.65 (d, J = 7.9 Hz, 1H), 5.28 – 4.89 (m, 2H), 4.35 (m, 1H), 3.61 (m, 2H), 2.57 (t, J= 7.5 Hz, 2H), 1,90(m, 1H), 1.67 (m, 5H), 1.43 (m, 2H), 1.22 (m, 21H), 0.86 (t, J = 6.7 Hz, 3H). LCMS (ESI) calcd.ForC34H52N304S [M+H]+598.36, obsd. 598.25

Synthesis of YC8-02—As in Figure S8B, compound 2 was synthesized following a procedure described in the literature(He et al., 2014).To a solution of compound 2(110 mg, 0.185mmol) and N-methylmorpholine (24.0 μl, 0.22 mmol) in dry dichloromethane (1.85 ml), isobutylchloroformate (31.0 μl, 0.22 mmol) was added dropwisely at 0°C. The reaction mixture was stirred for 30 min at 0°C. 3-Aminophenol (24 mg, 0.22mmol) was then added at 0°C and the reaction mixture was stirred for 16 h at room temperature. The solvent was removed under reduced pressure and the resulting residue was dissolved with EtOAc (40 ml) and washed with brine (20 ml). The organic layer was dried over anhydrous sodium sulfate. After removal of the solvents in vacuum, the residue was purified by flash chromatography on silica gel (hexanes:EtOAc = 1:1) to afford the expected compound3(67 mg, 53 % yield).Compound 3 was deprotected using 20 % piperidine in DCM (1 ml) for 2 h at room temperature. The solvent was removed under reduced pressure and the resulting residue was dissolved with EtOAc (40 ml) and washed with brine (20 ml). The organic layer was dried over anhydrous sodium sulfate. After removal of the solvents in vacuum, the residue was purified by flash chromatography on silica gel (DCM:MeOH = 85:15) to afford deprotected compound. To a solution of the resulting deprotected compound in DMF (0.5 ml) was added diisopropylethylamine (28.0μl, 0.2 mmol) and (2-Bromoethyl) triphenylphosphonium bromide (54 mg, 0.12mmol). The reaction mixture was stirred for 2 h at room temperature. The mixture was extracted with EtOAc (40 ml) and washed with brine (20 ml). The organic layer was dried over anhydrous sodium sulfate. After removal of the solvents in vacuum, the residue was purified by flash chromatography on silica gel (DCM:MeOH = 9:1) to afford the expected compound YC8-02 (13 mg, 17 % yield). 1H NMR (400 MHz, CDCb): δ 10.38 (s, 1H), 9.47 (s, 1H), 7.93 – 7.39 (m, 18H), 7.13 (d, J = 8.0 Hz, 1H), 6.95 (t, J = 8.0 Hz, 1H), 6.57 (dd, J = 8.1,2.1 Hz, 1H), 4.04 – 3.79 (m, 1H), 3.61 (s, 2H), 3.53 – 3.43 (m, 2H), 3.04 – 2.78 (m, 2H), 2.70 (dd, J = 9.0, 6.4 Hz, 2H), 1.82 – 1.43 (m, 4H), 1.37 – 1.09 (m, 24H), 0.84 (t, J = 6.7 Hz, 3H).LCMS (ESI) calcd. ForC46H63N302PS+ [M]+752.44, obsd. 752.51.

HPLC-based inhibition assay of sirtuins—Different concentrations (0.686, 2.058, 6.173, 18.519, 55.556, 166.667μM) of small molecule inhibitors were pre-incubated with 0.3 μM sirtuins (SIRT1, SIRT2, and SIRT3) and 1 mM NAD in buffer (20 mM Tris-HCI, pH 8.0, 1 mM DTT) at 37 °C for 10 min. Then 10 μM of acyl peptide (KQTARK(Ac)STGGWW)was added to initiate the reactions. The reactions were then incubated at 37°C in a total volume of 60 μl (5 min for SIRT1 and SIRT2, 20 min for SIRT3). The conversion of each reaction was less than 20%.The reactions were stopped by adding 60 μl of an aqueous solution of 50% methanol containing 200 mM HCI and 320 mM acetic acid. The reaction mixtures were then centrifuged at 17000g for 10 min and analyzed on an analytical HPLC with Kinetex 5u EVO C18 100A column (100 mm × 4.60 mm, 5.0 μm, Phenomenex). The gradient was: 0% B for 2 min, 0 to 30% B in 13 min, and then 30% to 100% B in 10 min at a flow rate of 0.5 ml/min. All reactions were done in duplicate. The product and the substrate peaks were quantified using HPLC UV absorption traces at 280 nm.

Drug uptake in mitochondria—Karpas 422 cells (1 million/ml) were treated with 3μM or 5μM JH-T4 or YC8-02 for 1 hour. 3 and 15 million cells were used for whole cell or mitochondria extraction respectively. Mitochondria were extracted using Qproteome

Mitochondria Isolation Kit (Qiagen). Whole cells or mitochondria pellets were lysed with ACN solution (Acetonitrile:H_2O, 2:1). 50 μL total cell lysates or mitochondria extracts were added to 50 μL acetonitrile and centrifuged at 17000g for 10 min to remove precipitated proteins. The supernatants were added to amide analogues for JH-T4 and YC8-02 as internal standards. The final concentration of internal standards was 40 nM and analyzed on LC-MS with positive mode for detection of mass-to-charge ratio of ions. The compound concentration was quantified by comparing the ion peak area of the inhibitors and corresponding internal standards. All solutions were done in duplicates.

Drug toxicity study and treatment in mice—YC8-02 was dissolved into DMSO at concentration of 36 mM as stock solution for *in vivo* toxicity and treatment study. To make drug solutions for intraperitoneal (IP) injection, we first mix drug stock solution with the same volume of Kolliphor® EL (Sigma-Aldrich), then add 8 volumes of PBS and mix well to make the final solutions for injection. The toxicity study was done with female C57BL/6J mice (3 months old). We set up 2 groups of mice to be injected with vehicle (DMSO, Kolliphor, PBS solution) and YC8-02 at 30 mg/kg. Each group had 3 mice. Each mouse was treated once per day for 5 days, and all mice were weighted every time before injections. Toxicity study stopped at day 8 (3 days after the last injection) after the last measurement of mice body weight. Mice body weight was used to evaluate the weight changes during and after treatment as shown in Figure S8J. *In vivo* DLBCL treatment study was carried out in NOD/SCID mice bearing xenografted DLBCL tumors. Tumor xenografts were done as describe above. Ten-week old female NOD/SCID mice housed in barrier environment were subcutaneously injected in the right flank with $7X10^6$ Karpas 422 cells. After about 2 and half weeks when the tumor volumes were around 100-200 mm^3, we randomly separate mice into two groups (each group n=4) for treatment via IP injection with vehicle and YC8-02 solution (30 mg/kg). Mice were treated once per day during week days for two weeks, and tumor volumes were monitored twice a week using electronic digital calipers in 2 dimensions. Tumor volume was calculated using the following formula: tumor volume (mm^3) = (smallest diameter^2 × largest diameter)/2. The experiment was stopped at 3 weeks after the first injection when control mice were reaching the maximal allowed tumor burden and tumor volumes used to generate Figure 8J.

QUANTIFICATION AND STATISTICAL ANALYSES

Survival analyses—Raw microarray data were downloaded from GEO at NCBI and annotated with Brainarray CDF annotation file(Dai et al., 2005). Different microarray data sets were combined after RMA normalization and the batch effects were adjusted with ComBat method(Johnson et al., 2007). The survival probability was estimated by Kaplan-Meier method and its association with gene expression was tested by log-rank test. Cox proportional hazard regression was used to calculate hazard ratio and to test association with gene expression while adjusting for clinical features. All analyses were performed using R packages from Bioconductor and statistical software SAS 9.4 (SAS Institute, Cary, NC).

Metabolomic analyses—Metabolomic data was obtained from Metabolon™ through untargeted metabolomic profiling using DLBCL cell lines or $B220^+$ cells isolated from mice. Data was preprocessed to exclude metabolites that contain missing values for ≥ 20%

and metabolite abundances were log-transformed and quantile normalized. Differentially abundant metabolites were determined using a linear model fit with moderated *t*-statistics from the *metabolomics* R package using a fold-change threshold of 1.2 and Benjamini-Hochberg adjusted p value <0.1 (De Livera et al., 2012; De Livera et al., 2015). Hierarchical clustering was performed on log-transformed metabolite data using Euclidean distance and Ward's method. Biological significance of the metabolomics signatures was assessed via over-representation or Wilcoxon enrichment analyses using Integrated Molecular Pathway Level Analysis (IMPaLA) (ref; http://impala.molgen.mpg.de).

DLBCL DNA copy number—Single nucleotide polymorphism (SNP) microarrays (Affymetrix 250k Sty; Affymetrix 250k Nsp; Affymetrix SNP6.0) and array comparative genome hybridization (CGH; Agilent 244k) arrays from previously studies(Bodker et al., 2013; Challa-Malladi et al., 2011; Compagno et al., 2009; Green et al., 2011; Kato et al., 2009; Lenz et al., 2008b; Monti et al., 2012)were downloaded from the gene expression omnibus (accessions, GSE34171, GSE12906, GSE15127, GSE37977, GSE22082, GSE11318;www.ncbi.nlm.nih.gov/geo/) or shared by the authors of the originating publication. All raw data were uniformly processed to generate Log2 copy number as previously described(Green et al., 2014), then segmented using the circular binary segmentation (CBS) module in GenePattern (Reich et al., 2006). Significant DNA copy number gains and losses were calculated using GISTIC2(Mermel et al., 2011) in GenePattern, with a DNA copy number change threshold of 0.1.

DLBCL gene expression analysis—Raw cel files for Affymetrix U133 plus 2.0 gene expression microarrays were obtained for 249 DLBCL tumors from previously published studies(Lenz et al., 2008a; Monti et al., 2012) via the gene expression gene expression omnibus (accessions GSE34171 and GSE10846; www.ncbi.nlm.nih.gov/qeo/). The data were RMA normalized using the ExpressionFileCreator module and batch corrected using the Com Bat module of GenePattern(Reich et al., 2006) (https://cloud.genepattern.org). The expression of genes was compared between diploid and 6q21 deleted cases using the average probe intensity and a Student's T-test.

Statistical analyses—A two-tailed Student's t test was used to determine the statistical significance of the results, p values ≤0.05 were considered statistically significant. Correlations were determined using Pearson correlation coefficients using GraphPad Prism. Log rank tests≤0.05 were standard for significance between subgroup of patients or animals.

DATA and SOFTWARE AVAILABILITY

RNA sequencing data from this paper have been deposited in the Gene Expression Omnibus (GEO) database. The accession numbers for the RNA sequencing data of GC B cells and DLBCL tumor cells are GSE45982 and GSE130751, respectively.

Supplementary Material

Refer to Web version on PubMed Central for supplementary material.

ACKNOWLEDGMENTS

We thank the Melnick lab for helpful discussions and suggestions, the Tri-lnstitutional Therapeutic Discovery Institute for help with the synthesis of small molecules. A.M. is supported by LLS SCOR 7012-16, a Falk Medical Research Catalyst Award, the Chemotherapy Foundation, and a TDI Institute Award and the Follicular Lymphoma Consortium.

REFERENCES

Alizadeh AA, Eisen MB, Davis RE, Ma C, Lossos IS, Rosenwald A, Boldrick JC, Sabet H, Tran T, Yu X, et al. (2000). Distinct types of diffuse large B-cell lymphoma identified by gene expression profiling. Nature 403, 503–511. [PubMed: 10676951]

Amengual JE, Clark-Garvey S, Kalac M, Scotto L, Marchi E, Neylon E, Johannet R, Wei Y, Zain J, and O'Connor OA (2013). Sirtuin and pan-class I/II deacetylase (DAC) inhibition is synergistic in preclinical models and clinical studies of lymphoma. Blood 122, 2104–2113. [PubMed: 23913470]

Baeza J, Smallegan MJ, and Denu JM (2016). Mechanisms and Dynamics of Protein Acetylation in Mitochondria. Trends Biochem Sci 41, 231–244. [PubMed: 26822488]

Basso K, and Dalla-Favera R (2015). Germinal centres and B cell lymphomagenesis. Nat Rev Immunol 15,172–184. [PubMed: 25712152]

Beguelin W, Popovic R, Teater M, Jiang Y, Bunting KL, Rosen M, Shen H, Yang SN, Wang L, Ezponda T, et al. (2013). EZH2 is required for germinal center formation and somatic EZH2 mutations promote lymphoid transformation. Cancer Cell 23, 677–692. [PubMed: 23680150]

Bell EL, Emerling BM, Ricoult SJ, and Guarente L (2011). SirT3 suppresses hypoxia inducible factor lalpha and tumor growth by inhibiting mitochondrial ROS production. Oncogene 30, 2986–2996. [PubMed: 21358671]

Bereshchenko OR, Gu W, and Dalla-Favera R (2002). Acetylation inactivates the transcriptional repressor BCL6. Nat Genet 32, 606–613. [PubMed: 12402037]

Bodker JS, Gyrup C, Johansen R, Schmitz A, Madsen J, Johnsen HE, Bogsted M, Dybkaer K, and Nyegaard M (2013). Performance comparison of Affymetrix SNP6.0 and cytogenetic 2.7M whole-genome microarrays in complex cancer samples. Cytogenet Genome Res 139, 80–87. [PubMed: 23182917]

Boothby M, and Rickert RC (2017). Metabolic Regulation of the Immune Humoral Response. Immunity 46, 743–755. [PubMed: 28514675]

Budczies J, Klauschen E, Sinn BV, Gyorffy B, Schmitt WD, Darb-Esfahani S, and Denkert C (2012). Cutoff Finder: a comprehensive and straightforward Web application enabling rapid biomarker cutoff optimization. PLoS One 7, e51862. [PubMed: 23251644]

Caro R, Kishan AU, Norberg E, Stanley IA, Chapuy B, Ficarro SB, Polak K, Tondera D, Gounarides J, Yin H, et al. (2012). Metabolic signatures uncover distinct targets in molecular subsets of diffuse large B cell lymphoma. Cancer Cell 22, 547–560. [PubMed: 23079663]

Chalkiadaki A, and Guarente L (2015). The multifaceted functions of sirtuins in cancer. Nat Rev Cancer 15, 608–624. [PubMed: 26383140]

Challa-Malladi M, Lieu YK, Califano O, Holmes AB, Bhagat G, Murty VV, Dominguez-Sola D, Pasqualucci L, and Dalla-Favera R (2011). Combined genetic inactivation of beta2-Microglobulin and CD58 reveals frequent escape from immune recognition in diffuse large B cell lymphoma. Cancer Cell 20, 728–740. [PubMed: 22137796]

Chapuy B, Stewart C, Dunford AJ, Kim J, Kamburov A, Redd RA, Lawrence MS, Roemer MGM, Li AJ, Ziepert M, et al. (2018). Molecular subtypes of diffuse large B cell lymphoma are associated with distinct pathogenic mechanisms and outcomes. Nat Med 24, 679–690. [PubMed: 29713087]

Chen Y, Fu LL, Wen X, Wang XY, Liu J, Cheng Y, and Huang J (2014). Sirtuin-3 (SIRT3), a therapeutic target with oncogenic and tumor-suppressive function in cancer. Cell Death Dis 5, e1047. [PubMed: 24503539]

Compagno M, Lim WK, Grunn A, Nandula SV, Brahmachary M, Shen Q, Bertoni E, Ponzoni M, Scandurra M, Califano A, et al. (2009). Mutations of multiple genes cause deregulation of NF-kappaB in diffuse large B-cell lymphoma. Nature 459, 717–721. [PubMed: 19412164]

Dai M, Wang P, Boyd AD, Rostov G, Athey B, Jones EG, Bunney WE, Myers RM, Speed TP, Akil H, et al. (2005). Evolving gene/transcript definitions significantly alter the interpretation of GeneChip data. Nucleic Acids Res 33, e175. [PubMed: 16284200]

De Livera AM, Dias DA, De Souza D, Rupasinghe T, Pyke J, Tull D, Roessner U, McConville M, and Speed TP (2012). Normalizing and integrating metabolomics data. Anal Chem 84, 10768–10776. [PubMed: 23150939]

De Livera AM, Sysi-Aho M, Jacob L, Gagnon-Bartsch JA, Castillo S, Simpson JA, and Speed TP (2015). Statistical methods for handling unwanted variation in metabolomics data. Anal Chem 87, 3606–3615. [PubMed: 25692814]

Dent AL, Shaffer AL, Yu X, Allman D, and Staudt LM (1997). Control of inflammation, cytokine expression, and germinal center formation by BCL-6. Science 276, 589–592. [PubMed: 9110977]

Dobin A, Davis CA, Schlesinger E, Drenkow J, Zaleski C, Jha S, Batut R, Chaisson M, and Gingeras TR (2013). STAR: ultrafast universal RNA-seq aligner. Bioinformatics 29,15–21. [PubMed: 23104886]

Egle A, Harris AW, Bath ML, O'Reilly L, and Coiy S (2004). VavP-Bcl2 transgenic mice develop follicular lymphoma preceded by germinal center hyperplasia. Blood 103, 2276–2283. [PubMed: 14630790]

Eisenberg T, Schroeder S, Andiyushkova A, Pendl T, Kuttner V, Bhukel A, Marino G, Pietrocola E, Harger A, Zimmermann A, et al. (2014). Nucleocytosolic depletion of the energy metabolite acetyl-coenzyme a stimulates autophagy and prolongs lifespan. Cell Metab 19, 431–444. [PubMed: 24606900]

Ersching J, Efeyan A, Mesin L, Jacobsen JT, Pasqual G, Grabiner BC, Dominguez-Sola D, Sabatini DM, and Victora GD (2017). Germinal Center Selection and Affinity Maturation Require Dynamic Regulation of mTORCl Kinase. Immunity 46,1045–1058 e1046. [PubMed: 28636954]

Finley LW, Carracedo A, Lee J, Souza A, Egia A, Zhang J, Teruya-Feldstein J, Moreira PI, Cardoso SM, Clish CB, et al. (2011). SIRT3 opposes reprogramming of cancer cell metabolism through HIF1alpha destabilization. Cancer Cell 19, 416–428. [PubMed: 21397863]

Ginet V, Puyal J, Rummel C, Aubry D, Breton C, Cloux AJ, Majjigapu SR, Sordat B, Vogel R, Bruzzone S, et al. (2014). A critical role of autophagy in antileukemia/lymphoma effects of AP0866, an inhibitor of NAD biosynthesis. Autophagy 10, 603–617. [PubMed: 24487122]

Green MR, Aya-Bonilla C, Gandhi MK, Lea RA, Wellwood J, Wood P, Marlton P, and Griffiths LR (2011). Integrative genomic profiling reveals conserved genetic mechanisms for tumorigenesis in common entities of non-Hodgkin's lymphoma. Genes Chromosomes Cancer 50, 313–326. [PubMed: 21305641]

Green MR, Vicente-Duenas C, Romero-Camarero I, Long Liu C, Dai B, Gonzalez-Herrero I, Garcia-Ramirez I, Alonso-Escudero E, Iqbal J, Chan WC, et al. (2014). Transient expression of Bcl6 is sufficient for oncogenic function and induction of mature B-cell lymphoma. Nat Commun 5, 3904. [PubMed: 24887457]

Gump JM, Staskiewicz L, Morgan MJ, Bamberg A, Riches DW, and Thorburn A (2014). Autophagy variation within a cell population determines cell fate through selective degradation of Fap-1. Nat Cell Biol 16, 47–54. [PubMed: 24316673]

Haigis MC, Deng CX, Finley LW, Kim HS, and Gius D (2012). SIRT3 is a mitochondrial tumor suppressor: a scientific tale that connects aberrant cellular ROS, the Warburg effect, and carcinogenesis. Cancer Res 72, 2468–2472. [PubMed: 22589271]

Hanahan D, and Weinberg RA (2011). Hallmarks of cancer: the next generation. Cell 144,646–674. [PubMed: 21376230]

He B, Hu J, Zhang X, and Lin H (2014). Thiomyristoyl peptides as cell-permeable Sirt6 inhibitors. Org Biomol Chem 12, 7498–7502. [PubMed: 25163004]

Hebert AS, Dittenhafer-Reed KE, Yu W, Bailey DJ, Selen ES, Boersma MD, Carson JJ, Tonelli M, Balloon AJ, Higbee AJ, et al. (2013). Calorie restriction and SIRT3 trigger global reprogramming of the mitochondrial protein acetylome. Mol Cell 49,186–199. [PubMed: 23201123]

Heltweg B, Gatbonton T, Schuler AD, Posakony J, Li H, Goehle S, Kollipara R, Depinho RA, Gu Y, Simon JA, and Bedalov A (2006). Antitumor activity of a small-molecule inhibitor of human silent information regulator 2 enzymes. Cancer Res 66, 4368–4377. [PubMed: 16618762]

Herranz D, Ambesi-Impiombato A, Sudderth J, Sanchez-Martin M, Belver L, Tosello V, Xu L, Wendorff AA, Castillo M, Haydu JE, et al. (2015). Metabolic reprogramming induces resistance to anti-NOTCHl therapies in T cell acute lymphoblastic leukemia. Nat Med 21,1182–1189. [PubMed: 26390244]

Hirschey MD, Shimazu T, Goetzman E, Jing E, Schwer B, Lombard DB, Grueter CA, Harris C, Biddinger S, Ilkayeva OR, et al. (2010). SIRT3 regulates mitochondrial fatty-acid oxidation by reversible enzyme deacetylation. Nature 464,121–125. [PubMed: 20203611]

Houtkooper RH, Pirinen E, and Auwerx J (2012). Sirtuins as regulators of metabolism and healthspan. Nat Rev Mol Cell Biol 13, 225–238. [PubMed: 22395773]

Hummel M, Bentink S, Berger H, Klapper W, Wessendorf S, Barth TE, Bernd HW, Cogliatti SB, Dierlamm J, Feller AC, et al. (2006). A biologic definition of Burkitt's lymphoma from transcriptional and genomic profiling. N Engl J Med 354, 2419–2430. [PubMed: 16760442]

Intlekofer AM, and Younes A (2014). Precision therapy for lymphoma-current state and future directions. Nat Rev Clin Oncol 11, 585–596. [PubMed: 25135367]

Jais JP, Haioun C, Molina TJ, Rickman DS, de Reynies A, Berger F, Gisselbrecht C, Briere J, Reyes F, Gaulard P, et al. (2008). The expression of 16 genes related to the cell of origin and immune response predicts survival in elderly patients with diffuse large B-cell lymphoma treated with CHOP and rituximab. Leukemia 22,1917–1924. [PubMed: 18615101]

Jellusova J, Cato MH, Apgar JR, Ramezani-Rad P, Leung CR, Chen C, Richardson AD, Conner EM, Benschop RJ, Woodgett JR, and Rickert RC (2017). Gsk3 is a metabolic checkpoint regulator in B cells. Nat Immunol 18, 303–312. [PubMed: 28114292]

Jing H, Hu J, He B, Negron Abril YL, Stupinski J, Weiser K, Carbonaro M, Chiang YL, Southard T, Giannakakou P, et al. (2016). A SIRT2-Selective Inhibitor Promotes c-Myc Oncoprotein Degradation and Exhibits Broad Anticancer Activity. Cancer Cell 29,767–768. [PubMed: 27165747]

Johnson WE, Li C, and Rabinovic A (2007). Adjusting batch effects in microarray expression data using empirical Bayes methods. Biostatistics 8,118–127. [PubMed: 16632515]

Kamburov A, Cavill R, Ebbels TM, Herwig R, and Keun HC (2011). Integrated pathway-level analysis of transcriptomics and metabolomics data with IMPaLA. Bioinformatics 27, 2917–2918. [PubMed: 21893519]

Kato M, Sanada M, Kato I, Sato Y, Takita J, Takeuchi K, Niwa A, Chen Y, Nakazaki K, Nomoto J, et al. (2009). Frequent inactivation of A20 in B-cell lymphomas. Nature 459, 712–716. [PubMed: 19412163]

Kenific CM, and Debnath J (2015). Cellular and metabolic functions for autophagy in cancer cells. Trends Cell Biol 25, 37–45. [PubMed: 25278333]

Kimmelman AC, and White E (2017). Autophagy and Tumor Metabolism. Cell Metab 25, 1037–1043. [PubMed: 28467923]

Klionsky DJ, Abdelmohsen K, Abe A, Abedin MJ, Abeliovich H, Acevedo Arozena A, Adachi H, Adams CM, Adams PD, Adeli K, et al. (2016). Guidelines for the use and interpretation of assays for monitoring autophagy (3rd edition). Autophagy 12,1–222. [PubMed: 26799652]

Le A, Lane AN, Hamaker M, Bose S, Gouw A, Barbi J, Tsukamoto T, Rojas CJ, Slusher BS, Zhang H, et al. (2012). Glucose-independent glutamine metabolism via TCA cycling for proliferation and survival in B cells. Cell Metab 15,110–121. [PubMed: 22225880]

Lenz G, Wright G, Dave SS, Xiao W, Powell J, Zhao H, Xu W, Tan B, Goldschmidt N, Iqbal J, et al. (2008a). Stromal gene signatures in large-B-cell lymphomas. N Engl J Med 359, 2313–2323. [PubMed: 19038878]

Lenz G, Wright GW, Emre NC, Kohlhammer H, Dave SS, Davis RE, Carty S, Lam LT, Shaffer AL, Xiao W, et al. (2008b). Molecular subtypes of diffuse large B-cell lymphoma arise by distinct genetic pathways. Proc Natl Acad Sci U S A 105,13520–13525. [PubMed: 18765795]

Liao Y, Smyth GK, and Shi W (2013). The Subread aligner: fast, accurate and scalable read mapping by seed-and-vote. Nucleic Acids Res 41, e108. [PubMed: 23558742]

Liu K, Lee J, Kim JY, Wang L, Tian Y, Chan ST, Cho C, Machida K, Chen D, and Ou JJ (2017). Mitophagy Controls the Activities of Tumor Suppressor p53 to Regulate Hepatic Cancer Stem Cells. Mol Cell 68, 281–292 e285. [PubMed: 29033320]

Lombard DB, Alt FW, Cheng HL, Bunkenborg J, Streeper RS, Mostoslavsky R, Kim J, Yancopoulos G, Valenzuela D, Murphy A, et al. (2007). Mammalian Sir2 homolog SIRT3 regulates global mitochondrial lysine acetylation. Mol Cell Biol 27, 8807–8814. [PubMed: 17923681]

Luo J, Solimini NL, and Elledge SJ (2009). Principles of cancer therapy: oncogene and non-oncogene addiction. Cell 136, 823–837. [PubMed: 19269363]

Mahajan SS, Scian M, Sripathy S, Posakony J, Lao U, Loe TK, Leko V, Thalhofer A, Schuler AD, Bedalov A, and Simon JA (2014). Development of pyrazolone and isoxazol-5-one cambinol analogues as sirtuin inhibitors. J Med Chem 57, 3283–3294. [PubMed: 24697269]

Marino G, Pietrocola F, Eisenberg T, Kong Y, Malik SA, Andiyushkova A, Schroeder S, Pendl T, Harger A, Niso-Santano M, et al. (2014). Regulation of autophagy by cytosolic acetyl-coenzyme A. Mol Cell 53, 710–725. [PubMed: 24560926]

Martinez-Reyes I, Diebold LP, Kong H, Schieber M, Huang H, Hensley CT, Mehta MM, Wang T, Santos JH, Woychik R, et al. (2016). TCA Cycle and Mitochondrial Membrane Potential Are Necessary for Diverse Biological Functions. Mol Cell 61,199–209. [PubMed: 26725009]

Mathew R, Khor S, Hackett SR, Rabinowitz JD, Perlman DH, and White E (2014). Functional role of autophagy-mediated proteome remodeling in cell survival signaling and innate immunity. Mol Cell 55, 916–930. [PubMed: 25175026]

Mermel CH, Schumacher SE, Hill B, Meyerson ML, Beroukhim R, and Getz G (2011). GISTIC2.0 facilitates sensitive and confident localization of the targets of focal somatic copy-number alteration in human cancers. Genome Biol 12, R41. [PubMed: 21527027]

Mesin L, Ersching J, and Victora GD (2016). Germinal Center B Cell Dynamics. Immunity 45, 471–482. [PubMed: 27653600]

Monti S, Chapuy B, Takeyama K, Rodig SJ, Hao Y, Yeda KT, Inguilizian H, Mermel C, Currie T, Dogan A, et al. (2012). Integrative analysis reveals an outcome-associated and targetable pattern of p53 and cell cycle deregulation in diffuse large B cell lymphoma. Cancer Cell 22, 359–372. [PubMed: 22975378]

Monti S, Savage KJ, Kutok JL, Feuerhake F, Kurtin P, Mihm M, Wu B, Pasqualucci L, Neuberg D, Aguiar RC, et al. (2005). Molecular profiling of diffuse large B-cell lymphoma identifies robust subtypes including one characterized by host inflammatory response. Blood 105,1851–1861. [PubMed: 15550490]

Nahimana A, Attinger A, Aubry D, Greaney P, Ireson C, Thougaard AV, Tjornelund J, Dawson KM, Dupuis M, and Duchosal MA (2009). The NAD biosynthesis inhibitor AP0866 has potent antitumor activity against hematologic malignancies. Blood 113, 3276–3286. [PubMed: 19196867]

Noda NN, and Inagaki F (2015). Mechanisms of Autophagy. Annu Rev Biophys 44,101–122. [PubMed: 25747593]

Oberdoerffer R, Michan S, McVay M, Mostoslavsky R, Vann J, Park SK, Hartlerode A, Stegmuller J, Hafner A, Loerch R, et al. (2008). SIRT1 redistribution on chromatin promotes genomic stability but alters gene expression during aging. Cell 135, 907–918. [PubMed: 19041753]

Pavlova NN, and Thompson CB (2016). The Emerging Hallmarks of Cancer Metabolism. Cell Metab 23, 27–47. [PubMed: 26771115]

Pietrocola E, Pol J, Vacchelli E, Rao S, Enot DP, Baracco EE, Levesque S, Castoldi E, Jacquelot N, Yamazaki T, et al. (2016). Caloric Restriction Mimetics Enhance Anticancer Immunosurveillance. Cancer Cell 30,147–160. [PubMed: 27411589]

Reddy A, Zhang J, Davis NS, Moffitt AB, Love CL, Waldrop A, Leppa S, Pasanen A, Meriranta L, Karjalainen-Lindsberg ML, et al. (2017). Genetic and Functional Drivers of Diffuse Large B Cell Lymphoma. Cell 171, 481–494 e415. [PubMed: 28985567]

Reich M, Liefeld T, Gould J, Lerner J, Tamayo R, and Mesirov JP (2006). GenePattern 2.0. Nat Genet 38, 500–501. [PubMed: 16642009]

Schroeder S, Pendl T, Zimmermann A, Eisenberg T, Carmona-Gutierrez D, Ruckenstuhl C, Marino G, Pietrocola E, Harger A, Magnes C, et al. (2014). Acetyl-coenzyme A: a metabolic master regulator of autophagy and longevity. Autophagy 10,1335–1337. [PubMed: 24904996]

Shaknovich R, Geng H, Johnson NA, Tsikitas L, Cerchietti L, Greally JM, Gascoyne RD, Elemento O, and Melnick A (2010). DNA methylation signatures define molecular subtypes of diffuse large B-cell lymphoma. Blood 116, e81–89. [PubMed: 20610814]

Son J, Lyssiotis CA, Ying H, Wang X, Hua S, Ligorio M, Perera RM, Ferrone CR, Mullarky E, Shyh-Chang N, et al. (2013). Glutamine supports pancreatic cancer growth through a KRAS-regulated metabolic pathway. Nature 496,101–105. [PubMed: 23535601]

Szulc J, Wiznerowicz M, Sauvain MO, Trono D, and Aebischer P (2006). A versatile tool for conditional gene expression and knockdown. Nat Methods 3,109–116. [PubMed: 16432520]

Takamura A, Komatsu M, Hara T, Sakamoto A, Kishi C, Waguri S, Eishi Y, Hino O, Tanaka K, and Mizushima N (2011). Autophagy-deficient mice develop multiple liver tumors. Genes Dev 25, 795–800. [PubMed: 21498569]

Tao R, Coleman MC, Pennington JD, Ozden O, Park SH, Jiang H, Kim HS, Flynn CR, Hill S, Hayes McDonald W, et al. (2010). Sirt3-mediated deacetylation of evolutionarily conserved lysine 122 regulates MnSOD activity in response to stress. Mol Cell 40, 893–904. [PubMed: 21172655]

Yang H, Yang T, Baur JA, Perez E, Matsui T, Carmona JJ, Lamming DW, Souza-Pinto NC, Bohr VA, Rosenzweig A, et al. (2007). Nutrient-sensitive mitochondrial NAD+ levels dictate cell survival. Cell 130,1095–1107. [PubMed: 17889652]

Yang W, Nagasawa K, Munch C, Xu Y, Satterstrom K, Jeong S, Hayes SD, Jedrychowski MR, Vyas FS, Zaganjor E, et al. (2016). Mitochondrial Sirtuin Network Reveals Dynamic SIRT3-Dependent Deacetylation in Response to Membrane Depolarization. Cell 167, 985–1000 el021. [PubMed: 27881304]

Yu W, Denu RA, Krautkramer KA, Grindle KM, Yang DT, Asimakopoulos E, Hematti P, and Denu JM (2016). Loss of SIRT3 Provides Growth Advantage for B Cell Malignancies. J Biol Chem 291, 3268–3279. [PubMed: 26631723]

Yuan H, He M, Cheng F, Bai R, da Silva SR, Aguiar RC, and Gao SJ (2017). Tenovin-6 inhibits proliferation and survival of diffuse large B-cell lymphoma cells by blocking autophagy. Oncotarget 8,14912–14924. [PubMed: 28118604]

Significance

We still lack knowledge and targets to treat highly aggressive and heterogeneous DLBLCs. In this study, we discovered that reduced SIRT3 expression inhibited cell proliferation in different subtypes of DLBCLs cells, impaired lymphomagenesis in *VavP-Bcl2* mouse lymphoma model and was associated with better survival in human DLBCL patients. Though metabolomic profiling and metabolic tracing study, we found that SIRT3 maintained DLBCLs' metabolism by potentiating the TCA cycle through anaplerotic glutaminolysis. These findings prompted us to develop a mitochondria-targeting SIRT3 inhibitor, YC8-02, to treat diseases like DLBCLs, since SIRT3 expression is dispensable for tissue homeostasis under normal conditions.

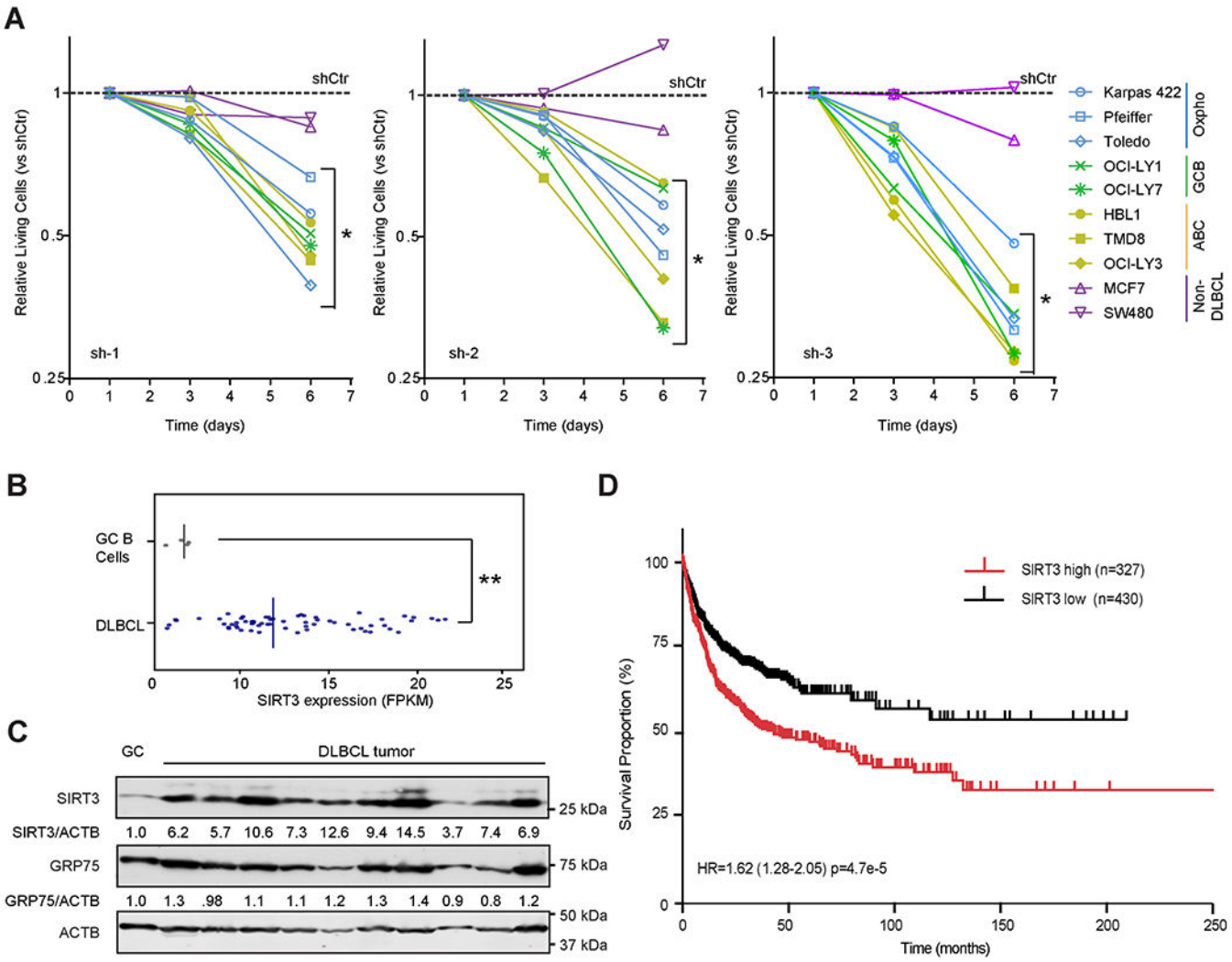

Figure 1. SIRT3 is Highly Expressed in DLBCL and Linked to Unfavorable Outcome.

(A) Effect of SIRT3 shRNAs on the proliferation of DLBCL and non-DLBCL cell lines. Each cell line was infected with lentivirus expressing control or SIRT3 shRNA and YFP. YFP^+ viable ($DAPI^-$) cells were monitored by flow-cytometry for 6 days. Data were normalized to cells transduced with control shRNA (dashed line).

(B) SIRT3 mRNA expression detected by RNA-seq and indicated by FPKM (Fragment Per Kilobase Million) value in GC B cells (n=4) and primary DLBCL tumor samples (n=56). The median values of SIRT3 mRNA expression (the vertical line) were shown in the plot.

(C) Immunobloting for SIRT3 in primary DLBCL samples and purified human tonsillar GC B cells. GRP75 and ACTB were used as loading controls for mitochondrial and total protein, respectively. Densitometry results are indicated below the respective images.

(D) Kaplan-Meier overall survival analysis of DLBCL patients whose tumors express high (n=327) or low (n=430) SIRT3.

*p value<0.05, **p value<0.01, ***p value <0.001. Error bars represent the mean +/− SD of three or more replicates. See also Figure S1.

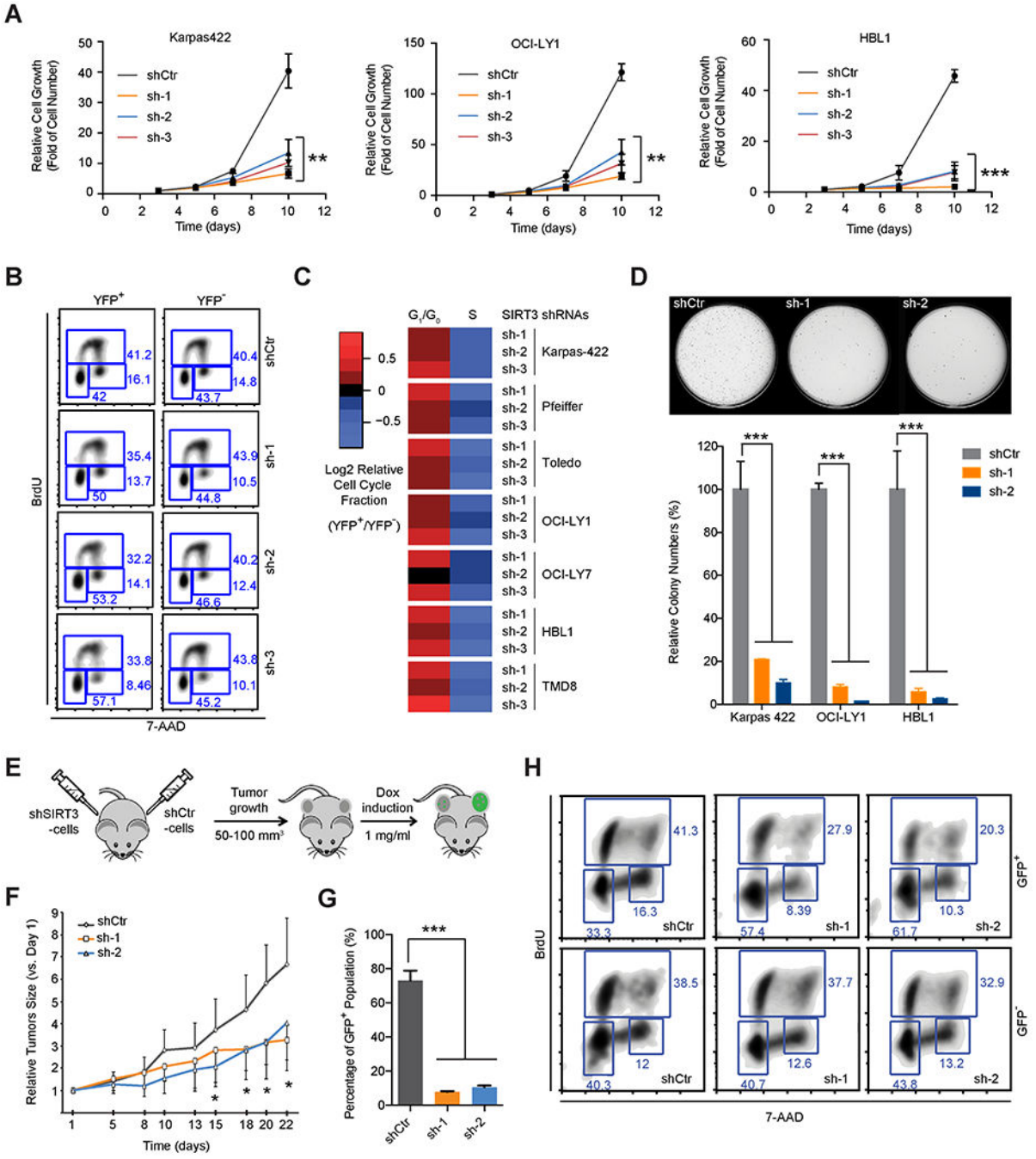

Figure 2. SIRT3 Expression Sustains DLBCL Proliferation and Survival *In vitro* and *In vivo*

(A) Growth curves of DLBCL cell lines with SIRT3 or control shRNAs. Relative cell growth represents the fold increase of cell numbers normalized to that from first time point (the third day post transduction).

(B) Cell cycle analysis of Karpas 422 cells with SIRT3 or control shRNAs using BrdU and 7AAD staining. YFP^+ and YFP^- cells represent infected and non-infected cells respectively co-cultured in the same flask.

(C) Heatmap summarizing cell cycle changes induced by SIRT3 shRNAs in DLBCL cell lines. The color scale reflects the Log2 relative cell cycle fractions (YFP^+/YFP^-), calculated by comparing the cell cycle profiles of YFP^+ and YFP^- in the same flasks.
(D) Photomicrographs (top) and quantification (bottom) of colony formation in SIRT3 or control shRNA transduced Karpas 422 cells after 14 days in culture.
(E) Schema of xenograft studies with inducible SIRT3 or control shRNA expressing cells.
(F) Growth curves of xenografted tumors (Karpas 422) after induction of control or SIRT3 shRNAs expression with doxycycline *in vivo.* Relative tumor volumes were calculated by normalizing against the tumor volume at day one following doxycycline administration.
(G) Percentage of GFP^+ cells in xenografted tumors. Xenografted tumor cells were harvested at 3 weeks post-induction with doxycycline and analyzed by flow-cytometry.
(F) Cell cycle analyses performed after *in vivo* BrdU incorporation in xenografted tumors following induction of SIRT3 or control shRNA expression.
*p value<0.05, **p value<0.01, ***p value <0.001. Error bars represent the mean +/− SD of three or more replicates. See also Figure S2.

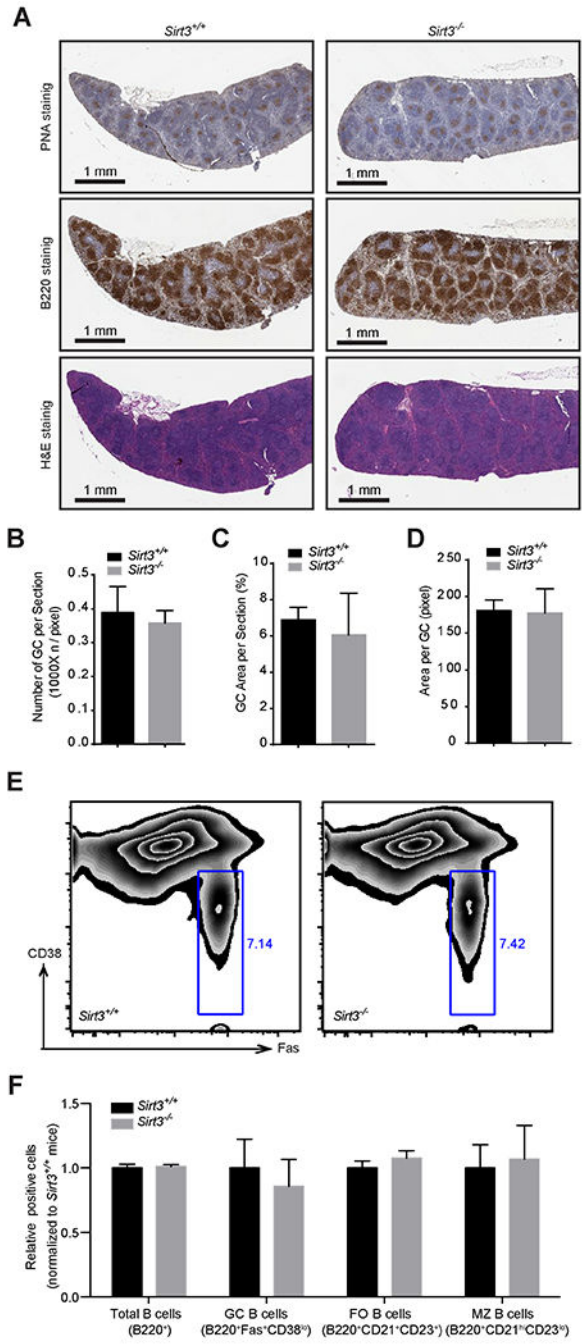

Figure 3. SIRT3 is Dispensable for GC B-cell Function *In vivo*

(A) PNA (top), B220 (middle) and hematoxylin and Eosin (FI&E) (bottom) staining of spleen sections derived from *Sirt3*$^{+/+}$ and *Sirt3*$^{-/-}$ mice.

(B) Numbers of GCs per spleen sections derived from *Sirt3*$^{+/+}$ and *Sirt3*$^{-/-}$ mice.

(C) Surface area of splenic sections occupied by GCs from *Sirt3*$^{+/+}$ and *Sirt3*$^{-/-}$ mice.

(D) Surface area of individual GCs in spleen sections from *Sirt3*$^{+/+}$ and *Sirt3*$^{-/-}$ mice.

(E) Flow cytometry to determine the relative abundance of GC B cells (CD38^{low}FAS^{+}, indicated by gating) in DAPI^{-}B220^{+} *Sirt3*$^{+/+}$ and *Sirt3*$^{-/-}$ splenocytes.

(F) Relative percentage total B cells, GC B cells, follicular (FO) B cells, and marginal zone (MZ) B cells from *Sirt3*$^{+/+}$ and *Sirt3*$^{-/-}$ splenocytes detected by immunophenotyping with the indicated stains.

Error bars represent the mean +/− SD of three or more replicates. See also Figure S3.

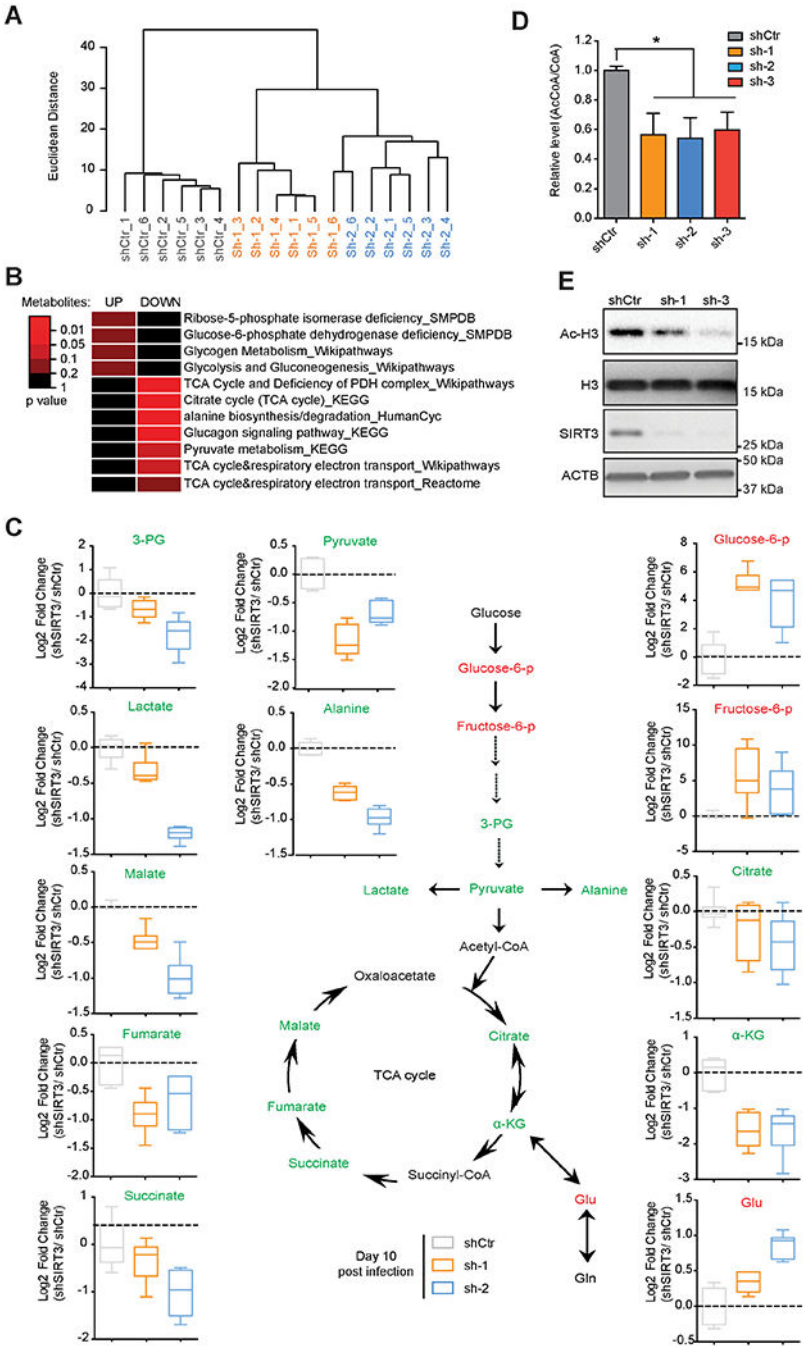

Figure 4. Loss of SIRT3 Impairs the TCA Cycle Metabolism

(A) Unsupervised hierarchical clustering of metabolomic profiles performed in SIRT3 or control shRNA transduced Karpas 422 at day 10 post-infection.

(B) Fleatmap showing significantly over-represented metabolic pathways among differential metabolites in Karpas 422 cells with SIRT3 shRNAs. The color key represents p values of metabolites enriched in various metabolic pathways (Wilcoxon test).

(C) Relative abundance of the indicated metabolites (z score, normalized to control) detected by metabolic profiling from Karpas 422 cells transduced with SIRT3 or control shRNAs.

Green, red and black text is used to indicate decreased, increased and no detection/change, respectively. Box plot represents lower quartile; median and upper quartile and whiskers show observed minimum and maximum values.

(D) AcCoA/total CoA ratios determined by LC/MS/MC in Karpas 422 cells expressing SIRT3 or control shRNAs. *p value<0.05. Error bars represent the mean +/− SD of three or more replicates.

(E) Western blot performed with Ac-H3 antibodies in Karpas 422 cells transduced with SIRT3 or control shRNAs. Total H3 and ACTB immunoblots were also performed as loading controls for histone and total protein respectively.

See also Figure S4.

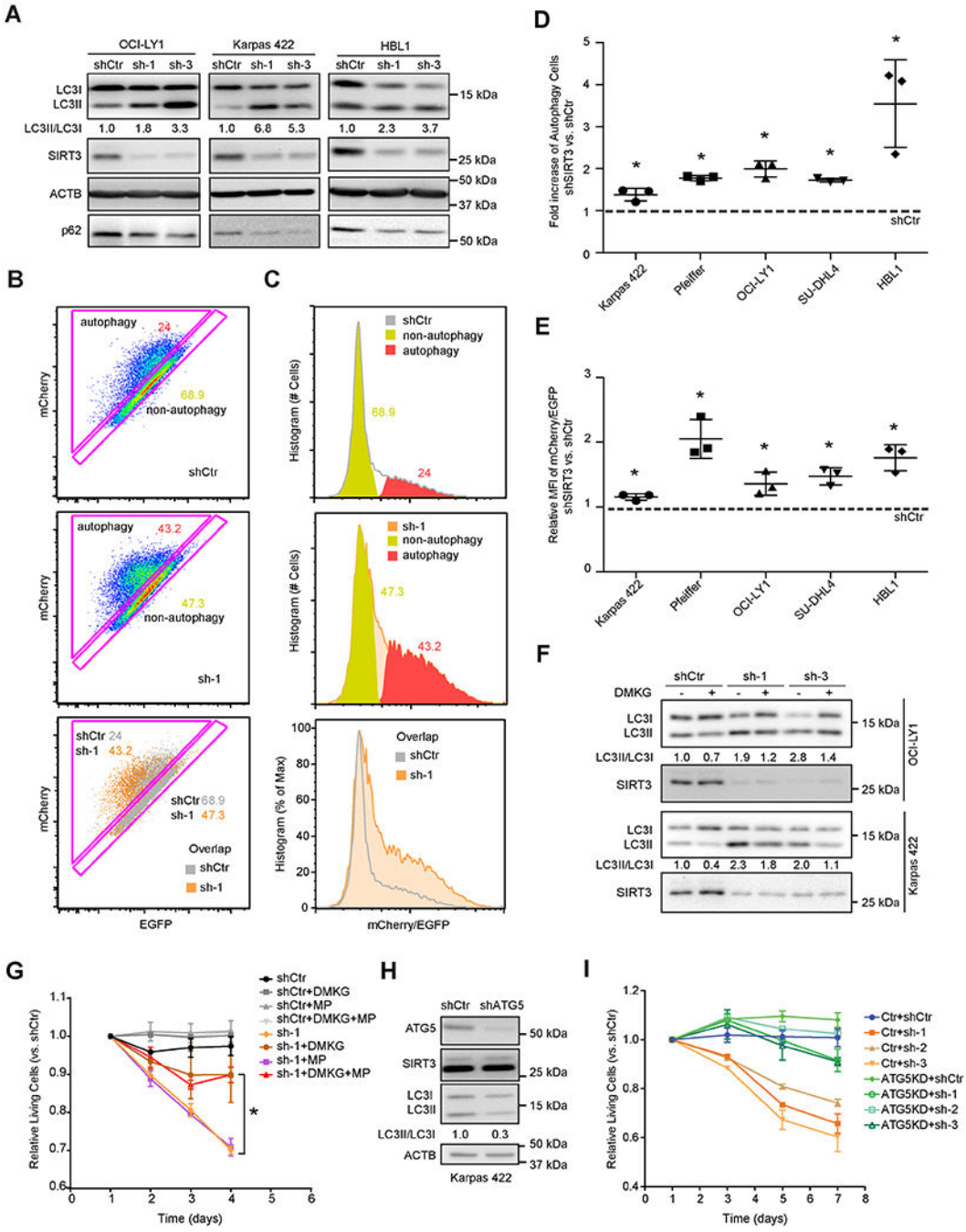

Figure 5. Loss of SIRT3 Activates Autophagy in DLBCL Cells

(A) Autophagy levels by detecting the ratio of LC3II/LC3I and p62 level in DLBCL cell lines with SIRT3 or control shRNAs. LC3II/LC3I ratios were quantified by densitometry and normalized to control shRNA (shCtr).

(B) Flow-cytometric analysis of DLBCL cells with a mCherry-EGFP-LC3 reporter showing autophagy activated (triangle) vs autophagy inactivated (along the diagonal) cells. Scatter plots of DLBCL cells transduced with shCtr (top), shSIRT3-sh-1 (middle), and their overlay (bottom) were shown.

(C) Representative histograms showing mCherry/EGFP signal from DLBCL cells transduced with shCtr (top), shSIRT3-sh-1 (middle) and their overlay (bottom). Red and yellow areas represent the signal intensities of mCherry/EGFP signals of autophagy active or inactive populations in Figure 5B, respectively.

(D) Fold changes of autophagy active cells in different DLBCL cell lines with SIRT3 shRNA vs control. The percentage of autophagy active populations, gated as Figure 5B, were used to calculate the fold increase of autophagy active cells in SIRT3 depleted vs controls cells (shSIRT3/shCtr).

(E) Fold changes of autophagy levels by comparing the mean fluorescence intensity (MFI) of mCherry/EGFP signal (calculated with histogram as in Figure 5C) in DLBCL cell lines with SIRT3 shRNA vs control (shSIRT3/shCtr).

(F) Effects of DMKG on autophagy (LC3II/LC3I) in DLBCL cells with SIRT3 or control shRNAs. Cells were incubated with DMKG (4 mM) for 3-4 hr before collecting for Western blot using LC3 or SIRT3 antibodies. LC3II/I ratios were calculated by densitometry and normalized to that of control cells.

(G) Effect of a 4-day exposure to DMKG, MP and both on the proliferation of Karpas 422 cells transduced with SIRT3 or control shRNA. The abundance of YFP^+ vs YFP^- (transduced vs non-transduced) cell populations were measured and normalized to the first time point.

(H) Karpas 422 cells were transduced with ATG5 or control shRNA and western blots performed using antibodies for ATG5, SIRT3, LC3, along with ACTB as loading controls. Densitometry was performed to determine the LC3II/LC3I ratios and normalized to that of control cells.

(I) Karpas 422 cells stable transfected with an ATG5 shRNA or control shRNA and selected by puromycin, then transduced with SIRT3 or control shRNA. Cell proliferation showed the relative abundance of YFP^+ vs YFP^- populations and normalized to the first time point

*p value<0.05. Error bars represent the mean +/− SD of three or more replicates. See also Figure S5.

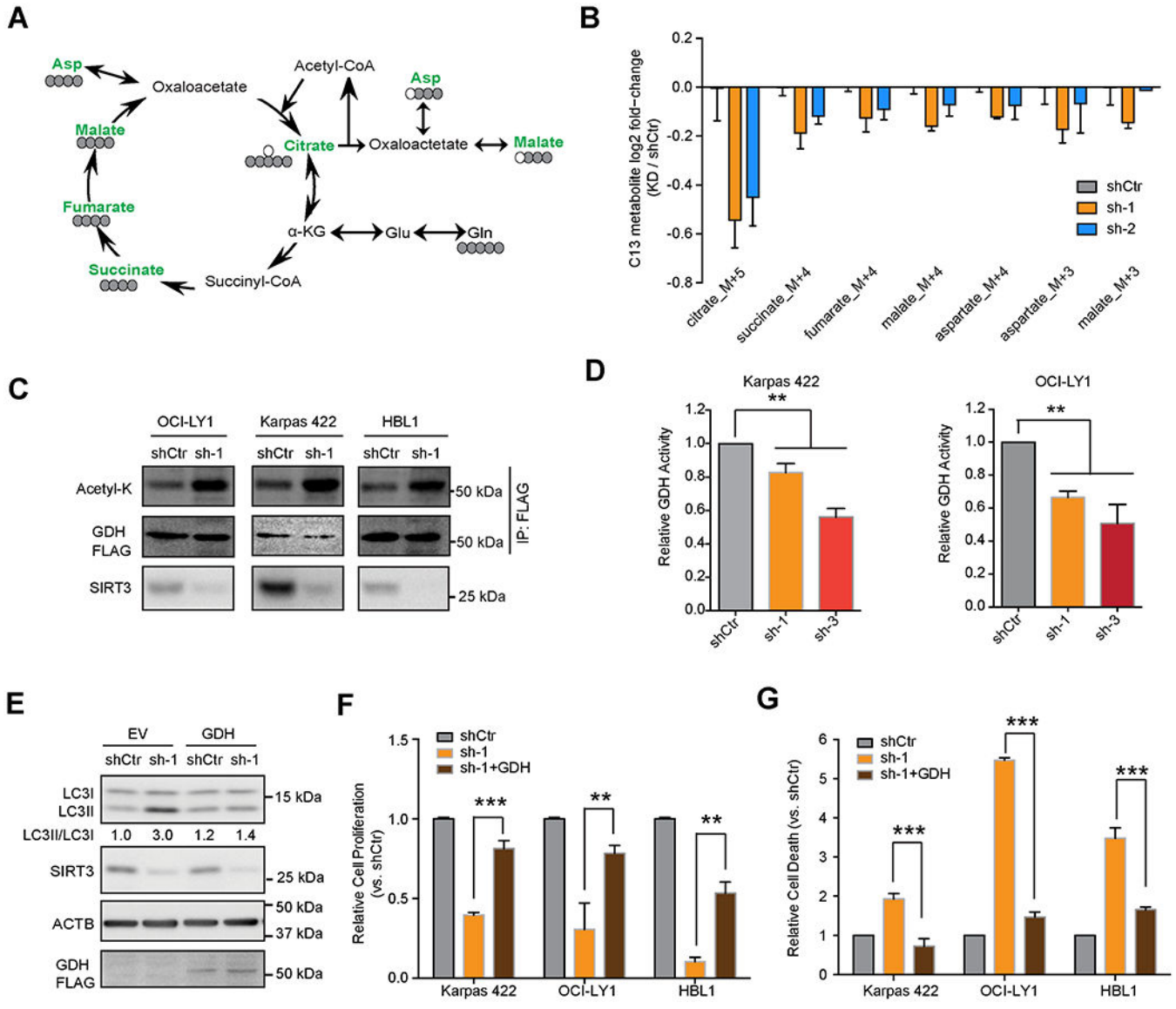

Figure 6. Glutamine Dehydrogenase is a Key Downstream Target of SIRT3 in DLBCL cells

(A) Karpas 422 cells were transduced with SIRT3 or control shRNA followed by exposure to [U-^{13}C5] glutamine. Color green indicates reduction and black indicates no change/ detection. Carbon atom (^{13}C in grey and ^{12}C in white circles) transitions and tracers were used to detect glutamine metabolism.

(B) Relative incorporation of ^{13}C glutamine in downstream metabolites in Karpas 422 cells. The Y-axis indicates log fold changes in ^{13}C-metabolites in cells transduced SIRT3 shRNA vs control.

(C) Acetylation levels of GDFI-FLAG in the indicated DLBCL cell lines with SIRT3 vs control shRNA. Immunoprecipitations followed by Western blots for acetyl-lysine (acetyl-K), GDH-FLAG (anti-FLAG).

(D) GDH activity was measured by GDH activity kit with cell lysates of Karpas 422 (left) and OCI-LY1 (right) DLBCL cells with SIRT3 or control shRNA. The Y axis shows the relative GDH activity normalized to that in control cells.

(E) Autophagy level (LC3II/LC3I) caused by SIRT3 shRNA (sh-1) in control (empty vector, EV) or exogenous GDH expressing cells (GDH). Densitometry results (LC3II/LC3I) were normalized to that in control cells (EV, shCtr cells).

(F) Relative cell numbers of control and SIRT3 depleted cells with or without co-expression of GDH. Results were normalized to cell numbers of controls (with control shRNA without GDH expression) at day 10 post-infection.

(G) Relative cell death in control or SIRT3 depleted cells with or without co-expression of GDH. The percentage of $DAPI^+$ cells were gated and normalized to controls (with control shRNA without GDH expression) at day 10 post-infection.

*p value<0.05, **p value<0.01, ***p value <0.001. Error bars represent the mean +/− SD of three or more replicates. See also Figure S6.

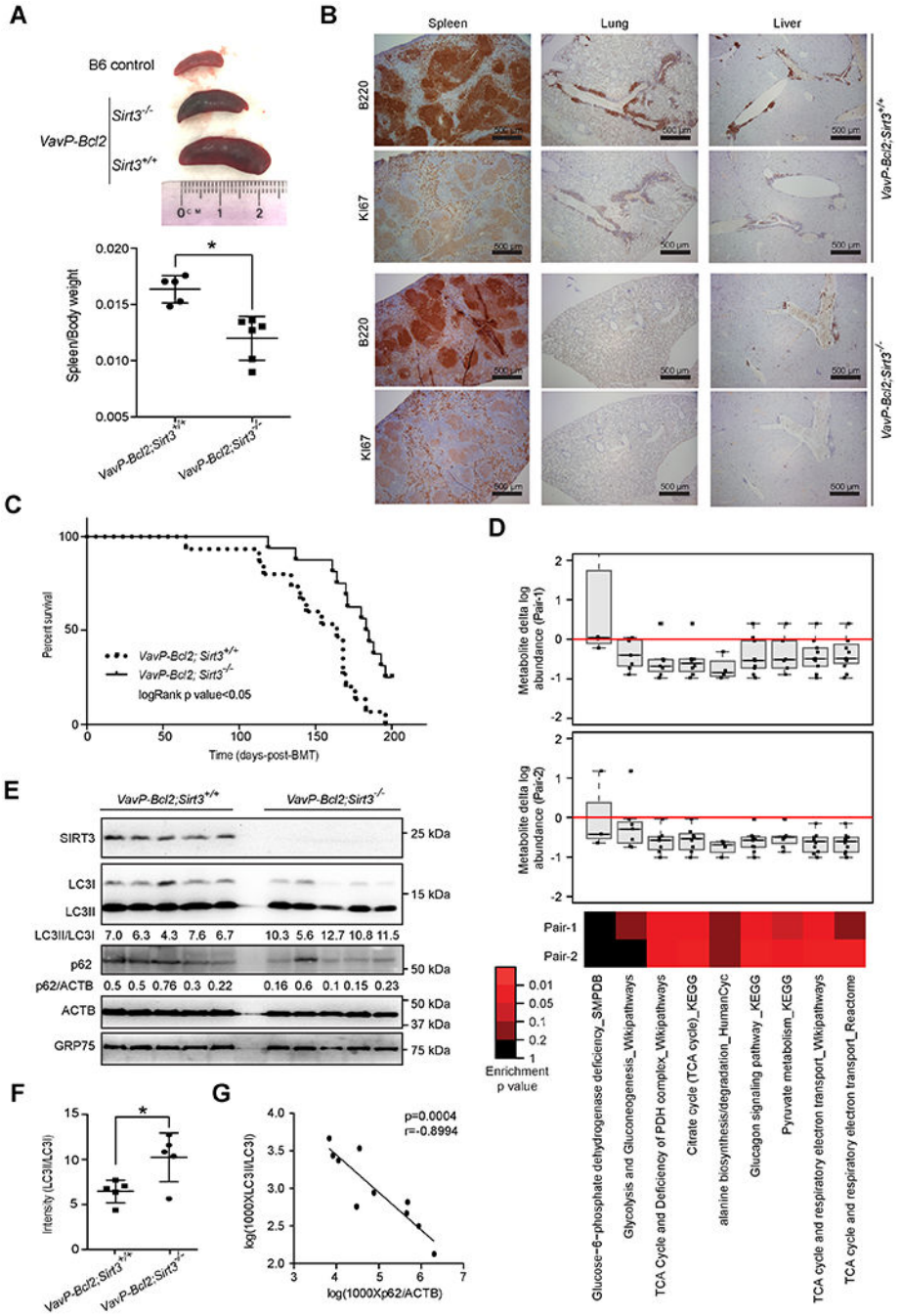

Figure 7. SIRT3 is Required for Lymphomagenesis

(A) Representative images of spleens from control C57B6/J(B6) mouse or recipient mice with *VavP-Bcl2;Sirt3*$^{+/+}$ or *VavP-Bcl2;Sirt3*$^{-/-}$ bone marrow cells at 110 days post bone marrow transplantation (top) and comparison of spleen/body weight ratios from mice with *VavP-Bcl2;Sirt3*$^{+/+}$ or *VavP-Bcl2;Sirt3*$^{-/-}$ bone marrow cells (bottom).

(B) H&E, B220 ,and Ki67 staining of spleen, lung and liver sections from mice transplanted with *VavP-Bcl2;Sirt3*$^{+/+}$ and *VavP-Bcl2;Sirt3*$^{-/-}$ bone marrow cells.

(C) Kaplan-Meier curve showing the overall survival of mice transplanted with *VavP-Bcl2;Sirt3*$^{+/+}$ (n=14) or *VavP-Bcl2;Sirt3*$^{-/-}$ (n=16) bone marrow cells.
(D) The box plots show relative change in metabolite abundance in *Sirt3*$^{-/-}$ vs *Sirt3*$^{+/+}$ lymphomas, and the heatmap shows statistical significance of these changes as determined by Wilcoxon test. Box plot represents lower quartile; median and upper quartile and whiskers show observed minimum and maximum values.
(E) Protein levels of SIRT3, LC3, p62 in splenocytes from *VavP-Bcl2;Sirt3*$^{+/+}$ or *VavP-Bcl2;Sirt3*$^{-/-}$ mice, GRP75 and ACTB were blotted as loading controls for mitochondrial and total protein respectively. The ratios of LC3II/LC3I and p62/ACTB were calculated with densitometry results.
(F) Quantification of LC3II/LC3I ratios in splenocytes from *VavP-Bcl2;Sirt3*$^{+/+}$ or *VavP-Bcl2;Sirt3*$^{-/-}$ mice based on densitometry results in (E).
(G) A correlation plot of p62/ACTB and LC3II/LC3I ratios in splenocytes of *VavP-Bcl2;Sirt3*$^{+/+}$ and *VavP-Bcl2;Sirt3*$^{-/-}$ mice, based on densitometry results in (E).
*p value<0.05. Error bars represent the mean +/− SD of three or more replicates. See also Figure S7.

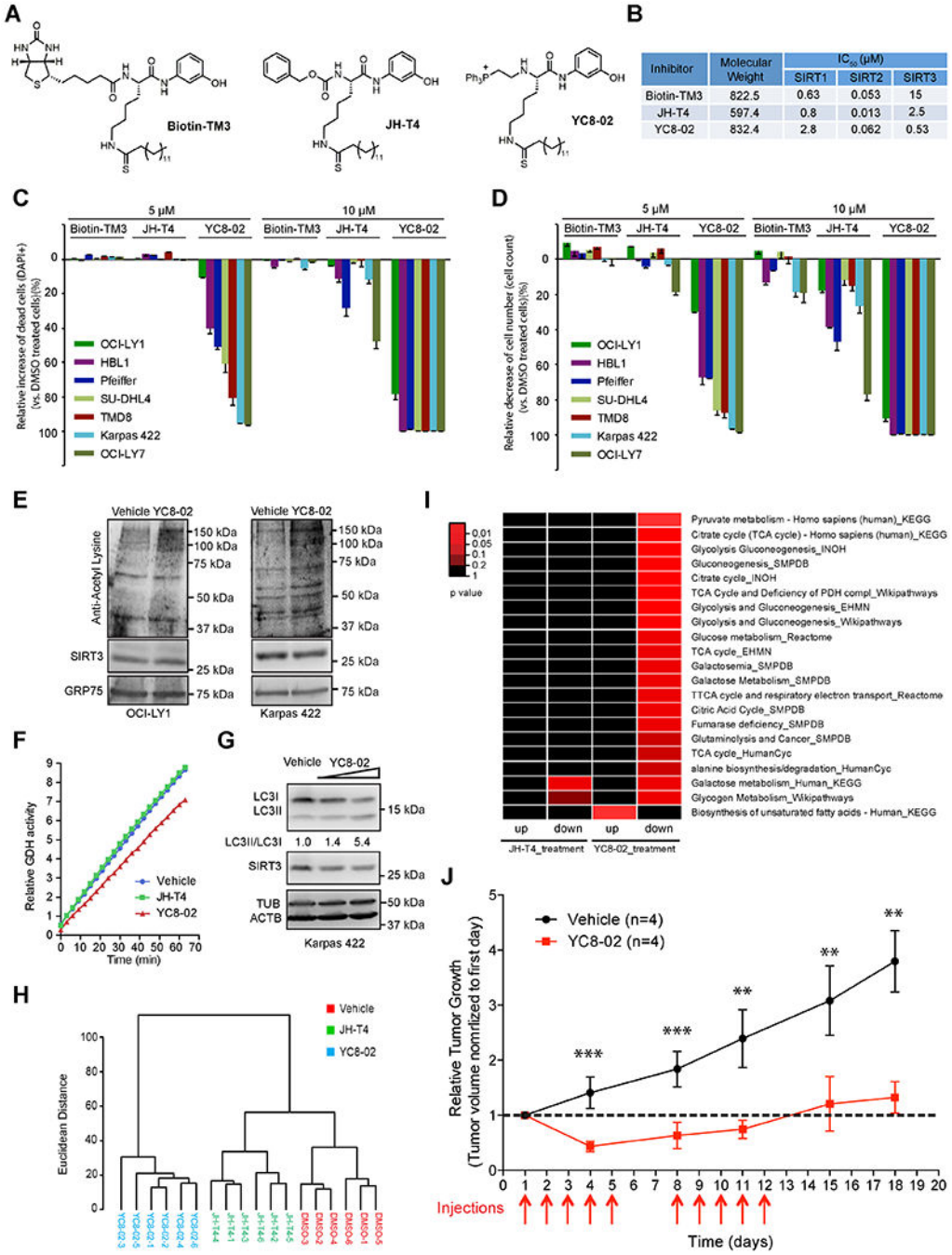

Figure. 8. Effects of SIRT3 inhibitor on the Metabolic Phenotype of DLBCL cells

(A) Chemical structures of Biotin-TM3, JH-T4, and YC8-02.

(B) Percentage of dead cells ($DAPI^+$) of DLBCL cell exposed to Biotin-TM3, JH-T4, and YC8-02 at 5 μM or 10 μM concentrations for 48 hr. Data were normalized to vehicle treated controls.

(C) Biochemical ICso values for Biotin-TM3, JH-T4, and YC8-02 were determined based on inhibition of deacetylase activities of SIRT1, SIR2 and SIRT3*in vitro*.

(D) Cell numbers changes of DLBCL cells treated with Biotin-TM3, JH-T4, and YC8-02 at 5 μM or 10 μM for 48 hr. Data were normalized to vehicle treated controls.
(E) Mitochondrial protein acetylation in OCI-LY1 and Karpas 422 cells (1 million/ml) treated with vehicle (DMSO) or YC8-02 at 7.5 μM and 5 μM, respectively. The mitochondrial protein fractions were enriched at 6 and 12 hr post treatment for Western blot using acetyl-lysine antibodies.
(F) GDH activity from cell lysates of Karpas 422 cells treated with 5 μM YC8-02, JH-T4 or vehicle for 48 hr. The Y axis shows the GDH activity in a time-lapse measurement.
(G) Autophagy levels (LC3II/LC3I) in Karpas 422 cells exposed to YC8-02 at 3 μM and 5 μM or vehicle for 40 hr. Densitometry was used to calculate LCII/I ratios normalized to that from vehicle treated control cells.
(H) Unsupervised hierarchical clustering of metabolomic profiles in Karpas 422 cells treated with vehicle (DMSO), JH-T4 or YC8-02.
(I) Heatmap showing significantly up or down-regulated metabolic pathways in Karpas 422 cells treated with JH-T4or YC8-02 vs vehicle controls. The color key indicates statistical significance based on the enrichment of metabolites in various pathways (Wilcoxon test).
(J) *In vivo* activity of YC8-02 against DLBCL xenografts. Treatments were done once per day for five days (weekdays) for two weeks (red arrows below x axis). Relative tumor volumes were calculated at the indicated timepoints by normalizing to the tumor volume of the first day prior to initiating treatment.
**p value < 0.01; ***p value< 0.001. Error bars represent the mean +/− SD of three or more replicates. See also Figure S8.

TABLE WITH EXAMPLES FOR AUTHOR REFERENCE

REAGENT or RESOURCE	SOURCE	IDENTIFIER
Antibodies		
SIRT3 antibody	Cell Signaling Technology	Cat#5940S
Beta-Actin antibody	Sigma-Aldrich	Cat#A5441-.2ML
B220 antibody for IHC	BD Bioscience	Cat#550286
KI67 antibody for IHC	Vector Laboratories	Cat#VP-K451
B220 antibody (FITC) for flow	BD Bioscience	Cat#553087
CD38 antibody (APC) for flow	ThermoFisher Scientific	Cat#17-0381-81
FAS/CD95 antibody (PE) for flow	BD Bioscience	Cat#557653
CD21 antibody (FITC) for flow	ThermoFisher Scientific	Cat#11-0212-81
CD23 antibody (PE) for flow	ThermoFisher Scientific	Cat#50-102-71
H3 Ac antibody	Cell Signaling Technology	Cat#8848S
H3 antibody	Millipore (Upstate)	Cat#09-838
LC3 antibody	Cell Signaling Technology	Cat#12741S
P62 antibody	Cell Signaling Technology	Cat#8025S
ATG5 antibody	Cell Signaling Technology	Cat#12994S
Ac-K antibody	Cell Signaling Technology; ImmuneChem	Cat#9441S; Cat#ICP0380
FLAG antibody	Sigma-Aldrich	Cat#F3165-MG
Grp75 antibody	Cell Signaling Technology	Cat#3593S
Beta-Tubulin antibody	Sigma-Aldrich	Cat#T6199-200UL
SIRT1 antibody	Cell Signaling Technology	Cat#9475P
SIRT2 antibody	Cell Signaling Technology	Cat#12650P
SIRT5 antibody	Cell Signaling Technology	Cat#8782P
SIRT6 antibody	Cell Signaling Technology	Cat#2590S
SIRT7 antibody	Cell Signaling Technology	Cat#5360P
GDH antibody	ProteinTech	Cat#14299-1-AP
Secondary antibody anti rabbit	Santa Cruz Biotechnology; Cell Signaling Technology	Cat#sc-2004; Cat#7074S
Secondary antibody anti mouse	Santa Cruz Biotechnology; Cell Signaling Technology	Cat#sc-2005; Cat#7076S
Anti-FLAG-beads	Sigma-Aldrich	Cat#A2220-5ML
Bacterial and Virus Strains		
pLKO.1-shScramble-puro/YFP	This paper	N/A
pLKO.1-shSIRT3-1-puro/YFP	MSKCC GES Core/this paper	TRCN0000038892
pLKO.1-shSIRT3-2-puro/YFP	This paper	N/A
pLKO.1-shSIRT3-3-puro/YFP	This paper	N/A
pLKO.1-shSIRT1-puro/YFP	MSKCC GES Core/this paper	TRCN0000018981
pLKO.1-shSIRT2-puro/YFP	MSKCC GES Core/this paper	TRCN0000040218
pLKO.1-shSIRT4-puro/YFP	MSKCC GES Core/this paper	TRCN0000018944

REAGENT or RESOURCE	SOURCE	IDENTIFIER
pLKO.1-shSIRT5-puro/YFP	MSKCC GES Core/this paper	TRCN0000018547
pLKO.1-shSIRT6-puro/YFP	MSKCC GES Core/this paper	TRCN0000050476
pLKO.1-shSIRT7-puro/YFP	MSKCC GES Core/this paper	TRCN0000020256
pLKO.1-shATG5-puro	MSKCC GES Core	TRCN0000151963
pLKO.1-shGDH-1-YFP	This paper	N/A
pLKO.1-shGDH-2-YFP	This paper	N/A
pLKO.1-shScramble-SIRT3m	This paper	N/A
pLKO.1-shScramble-SIRT3HYm	This paper	N/A
pLKO.1-shSIRT3-1-SIRT3m	This paper	N/A
pLKO.1-shSIRT3-2-SIRT3m	This paper	N/A
pLKO.1-shSIRT3-1-SIRT3HYm	This paper	N/A
pLKO.1-shSIRT3-2-SIRT3HYm	This paper	N/A
pLVUTH-KRAB-KM-shScramble	This paper	N/A
pLVUTH-KRAB-KM-shSIRT3-1	This paper	N/A
pLVUTH-KRAB-KM-shSIRT3-2	This paper	N/A
pLKO.1-shScramble-mCherry-GFP-LC3B-EF1-puro	This paper	N/A
pLKO.1-shSIRT3-mCherry-GFP-LC3B-EF1-puro	This paper	N/A
pLKO.1-shSramble-GDH1	This paper	N/A
pLKO.1-shSIRT3-1-GDH1	This paper	N/A
Biological Samples		
DLBCL tumor protein samples	Weill Cornell Medicine, Department of Pathology	N/A
Tonsils for B cell isolations	Weill Cornell Medicine, Department of Pathology	N/A
umbilical cord blood-derived	New York Blood Center (NYBC)	N/A
HSPCs (deidentified)		
Sheeps red blood in Alsevers (SRBC)	Cocalico Biological	Cat# 20-1334A
Chemicals, Peptides, and Recombinant Proteins		
Peanut Agglutinin Biotiny (PNA)	Vector Laboratories	Cat#B-1075
Hematoxylin Eosin	Vector Laboratories	Cat#H-3502
DAPI	Life Technologies	Cat#D3571
D-Glucose (U13C6, 99%)	Cambridge Isotope Laboratories, Inc.	CLM-1396-25-1
L-Glutamine (13C5, 99%)	Cambridge Isotope Laboratories, Inc.	CLM-1822-H-0.1
Dimethyl 2-oxoglutarate 96% (DMKG)	Sigma Aldrich	Cat#349631-5G
Methyl pyruvate 90%, technical grade (MP)	Sigma Aldrich	Cat#371173-25G
Biotin-TM3	This paper	N/A
JH-T4	This paper	N/A
YC8-02	This paper	N/A
Fetal Bovine Serum, Dialyzed	Life Technologies	Cat## 26400044
Kolliphor™ EL	Sigma Aldrich	Cat#C5135-500G

REAGENT or RESOURCE	SOURCE	IDENTIFIER
Recombinant SIRT1, SIRT2 and SIRT3 protein	This paper	N/A
In vitro assay substrate (AcH3K9 peptide)	This paper	N/A
NAD	VWR life Science	VWR 0455
Critical Commercial Assays		
MethoCult H4230	StemCell Technologies Inc.	Cat# 04230
BrdU staining kit	BD Biosciences	Cat#552598
GDH activity assay kit	BioVision	Cat#K729-100
Mitochondrial isolation kit	Qiagen; MilliporeSigma™	Cat#37612; Cat#QIA88-1KIT
CellTiter-Glo Luminescent Cell Viability Assay	Promega	Cat#G7573
CELL PROLIF DYE EF670	Thermo Fisher Scientific	Cat#65-0840-90
APC-Annexin V	BioLegend	Cat##640919
Deposited Data		
Raw data of gene expression and clinical information for survival analysis	Hummel et al., 2006	GEO:GSE4475
Raw data of gene expression and clinical information for survival analysis	Jais et al., 2008	ArrayExpress: E-TABM-346
Raw data of gene expression and clinical information for survival analysis	Lenz et al., 2008	GEO:GSE10846
Raw data of gene expression and clinical information for survival analysis	Shaknovich et al., 2010	GEO:GSE23501
Raw data for DNA copy number analysis	Monti et al., 2012	GEO:GSE34171
Raw data for DNA copy number analysis	Kato et al., 2009	GEO:GSE12906
Raw data for DNA copy number analysis	Compagno et al., 2009	GEO:GSE15127
Raw data for DNA copy number analysis	Bødker et al., 2013	GEO:GSE37977
Raw data for DNA copy number analysis	Green et al., 2011	GEO:GSE22082
Raw data for DNA copy number analysis	Lenz et al., 2008	GEO:GSE11318
Raw data of gene expression of GCB cells	Beguelin et al., 2013	GEO:GSE45982
Raw data of gene expression of DLBCL tumor cells	This paper	GEO:GSE130751
Experimental Models: Cell Lines		
OCI-LY1	Ontario Cancer Institute (OCI)	N/A
OCI-LY7	O Ontario Cancer Institute (OCI)	N/A
SUDHL-4	Deutsche Sammlung von Mikroorganismen und Zellkulturen (DSMZ)	ACC-495
Karpas 422	Deutsche Sammlung von Mikroorganismen und Zellkulturen (DSMZ)	ACC-32
Pfeiffer	American Type Culture Collection (ATCC)	CRL-2632
Toledo	American Type Culture Collection (ATCC)	CRL-2631
HBL1	Jose A. Martinez-Climent (Universidad de Navarra, Pamplona, Spain)	N/A
OCI-LY3	Ontario Cancer Institute (OCI)	N/A
TMD8	Louis M. Staudt (National Cancer Institute, Bethesda, Maryland, USA)	N/A
HEK-293T	American Type Culture Collection (ATCC)	CRL-1573

REAGENT or RESOURCE	SOURCE	IDENTIFIER
MCF7	American Type Culture Collection (ATCC)	HTB-22
SW480	American Type Culture Collection (ATCC)	CCL-228
Experimental Models: Organisms/Strains		
129S1	Jackson Laboratory	Stock No:002448
Sirt3 KO	Jackson Laboratory	Stock No:012755
SCID mouse	Jackson Laboratory	Stock No:001303
C57BL/6 (B6)	Jackson Laboratory	Stock No:000664
C57BL/6 (B6) CD45.1	Jackson Laboratory	Stock No:002014
VavP-Bcl2	Egle et al., 2004	N/A
VavP-Bcl2-sirt3$^{+/+}$	This paper	N/A
VavP-Bcl2-sirt3$^{-/-}$	This paper	N/A
Oligonucleotides		
shScramble:CAACAAGATGAAGAGCACCAA	This paper	N/A
shSIRT3-2:TTGCTGCATGTGGTTGAIIIC	This paper	N/A
shSIRT3-3:GGTGGAAGAAGGTCCATATCT	This paper	N/A
shGDH-1:GCCCTATGAAGGAAGCATCTT	This paper	N/A
shGDH-2:GCTGCCTATGTCAATGCCATT	This paper	N/A
Recombinant DNA		
pLVUTH-KRAB-KM	Szulc et al., 2006	N/A
pLKO.I-TRC vector	Addgene	10878
Software and Algorithms		
STAR	Dobin et al., 2013	http://github.com/alexdobin/STAR
Rsubread	Liao et al., 2013	http://bioconductor.org/packages/release/bioc/html/Rsebread.html
metabolomics	De Livera et al., 2012; De Livera et al., 2015	http://cran.r-proiect.org/packages=metabolomics
IMPaLA	Kamburov et al., 2011	http://impala.molgen.mpg.de
GenePattern	Reich et al., 2006	http://cloud.genepattern.org
Brainarray CDF	Dai et al., 2005	http://brainarray.mbni.med.umich.edu/Brainarray/Database/CustomCDF/genomic_curated_CDF.asp
Combat	Johnson et al., 2007	https://bioconductor.org/packages/release/bioc/html/sva.html
Cutoff finder	Budczies et al., 2012	http://molpath.charite.de/cutoff/
Flowjo	Flowjo	https://www.flowjo.com
ImageJ	ImageJ	https://imagei.nih.gov/ij/
GraphPad Prism 6.0	GraphPad Software	https://www.graphpad.com/